JGR

RESEARCH ARTICLE

Key Points:
- Anisotropy in mantle beneath South Island, New Zealand measured with *Pn* phases
- Finite strain within mantle lithosphere spread over a region of width 100–200 km
- Strain distribution matches deformation of a thin viscous sheet

Correspondence to:
J. A. Collins,
jcollins@whoi.edu

Pn anisotropy beneath the South Island of New Zealand and implications for distributed deformation in continental lithosphere

John A. Collins[1] and Peter Molnar[2]

[1]Department of Geology and Geophysics, Woods Hole Oceanographic Institution, Woods Hole, Massachusetts, USA, [2]Department of Geological Sciences, Cooperative Institute for Research in Environmental Sciences, University of Colorado Boulder, Boulder, Colorado, USA

Abstract *Pn* travel times from regional earthquakes recorded both by stations on New Zealand and by ocean bottom seismographs deployed offshore indicate anisotropy in the uppermost mantle beneath the region. The largest anisotropy of ~8% (±2%, 1σ) lies beneath the deforming part of the South Island to just off its West Coast, a zone roughly 100–200 km wide. The fastest propagation is aligned N60°E (±3°), essentially parallel to the largely strike-slip relative plate motion since 20 Ma, also ~ N60°E. The magnitude of anisotropy decreases abruptly northwest and southeast of this zone, and on the southeast side of the island, the orientation of fastest propagation is between N32°W and N-S. The ~ N60°E orientation of fast propagation is consistent with finite strain within the uppermost part of the mantle lithosphere if the measured 850 km of displacement of the Pacific plate past the Australia plate is spread over a region with a width of 100–200 km. The agreement of this orientation of fast propagation with the orientation or relative plate motion suggests the possibility of but does not require some dynamic recrystallization in rock as cold as 500–800°C, where Peierls creep seems to be the likely deformation mechanism. Such a strain distribution matches deformation of a thin viscous sheet that obeys a constitutive relationship of the form $\dot{\varepsilon} \sim \tau^n$, where $\dot{\varepsilon}$ is the average strain rate and τ is the operative deviatoric stress, with an average value of $n \approx 3$–10. Presumably, the NW-SE fast propagation in the region southeast of the island results from strain that precedes the Cenozoic deformation that has shaped the island.

1. Introduction

Faults divide the upper crust of continental regions into regions of mild deformation, if not effectively rigid "blocks," on geologic time scales. Perceptions of deformation in the underlying lower crust and uppermost mantle, however, differ. At one extreme, some imagine that the same rules that apply to plate tectonics—rigid plates of lithosphere—apply also to such continental blocks and that the faults cut through the entire crust and uppermost mantle to the asthenosphere. At the other extreme, some envision a continuously deforming lower crust and uppermost mantle, so that the blocks at the surface blur distributed deformation at depth.

Seismic anisotropy offers a test of these views. Olivine, the dominant mineral in the upper mantle, is strongly anisotropic in that *P* and *S* wave speeds vary by as much as 10% in different directions of propagation. Moreover, anisotropy develops easily during straining of olivine. Thus, the amount, orientation, and lateral extent of anisotropy can be compared with plausible distributions of finite strain to test whether deformation at depth is distributed over a wide or narrow zone beneath major faults.

Such tests require simple structures where strains are large enough for anisotropy to have developed. The South Island of New Zealand provides an ideal region for such a test. Relative plate motion has been largely strike slip for nearly 45 Ma, since the current phase of deformation began, and has been steady since ~20 Ma [e.g., *Cande and Stock*, 2004; *Sutherland*, 1995, 1999]. The total displacement of the Pacific plate past the Australia plate is constrained well at ~850 km [e.g., *Sutherland*, 1995, 1999], and most of that displacement has occurred since ~20 Ma [*Cande and Stock*, 2004]. In addition, two-thirds to three-quarters of the current GPS-measured relative plate motion is absorbed by slip on a single fault, the Alpine fault [*Beavan et al.*, 1999; *Norris and Cooper*, 2001; *Sutherland et al.*, 2006; *Wallace et al.*, 2007], and ~460 km of slip on the fault [e.g., *Sutherland*, 1995,
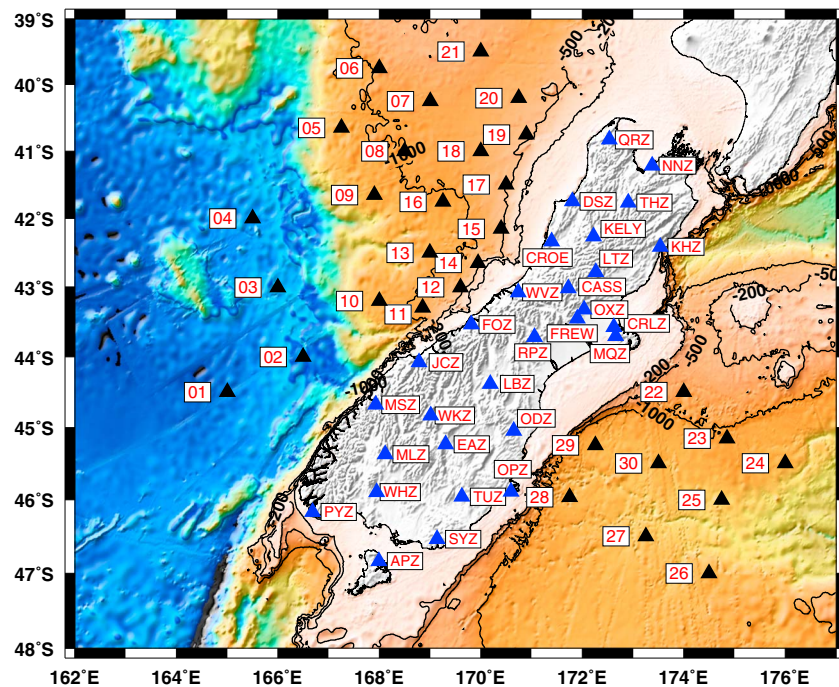
Figure 1. Map of seismic stations superimposed on bathymetry and topography. Ocean-bottom seismograph (OBS) and land stations are represented by the black and blue triangles, respectively. Stations NZ01–NZ04 lie on oceanic crust, but the other OBS stations (NZ05–NZ30) lie on thin continental crust. Stations CASS, CROE, FREW, and KELY, were temporary stations deployed specifically for the MOANA experiment. The remaining land stations are part of the New Zealand National Seismograph Network. Stations NZ02–NZ04, APZ, PYZ, NNZ, THZ, and KHZ were used to determine event corrections only. The vertical component of the seismometer deployed at NZ01 failed, and NZ17 was not recovered.

1999] shows that more than half of that 850 km of relative plate motion has occurred by slip on that fault. Accordingly, the average strain across the region can be estimated for any guess of the width of the deforming region, but some localization beneath the projection of the Alpine fault into the mantle seems likely.

Previous studies have demonstrated marked seismic anisotropy beneath the South Island of New Zealand. Shear wave splitting of core phases, like *SKS*, is large, and the orientations of the faster quasi-*S* waves are nearly parallel to the orientation of relative plate motion beneath the center of the island [e.g., *Duclos et al.*, 2005; *Klosko et al.*, 1999; *Savage et al.*, 2007a; *Zietlow et al.*, 2014]. Consistent with shear wave splitting, speeds of *Pn*, the *P* phase that propagates nearly horizontally in the uppermost mantle, also vary markedly with propagation direction, with the fastest *Pn* propagating roughly parallel to relative plate motion [*Baldock and Stern*, 2005; *Bourguignon et al.*, 2007; *Melhuish et al.*, 2005; *Scherwath et al.*, 2002]. These studies show a pattern of anisotropy in the upper mantle beneath the New Zealand region that is consistent with the expected strain field associated with the history of relative plate motion [e.g., *Little et al.*, 2002; *Molnar et al.*, 1999; *Moore et al.*, 2002; *Savage et al.*, 2007b]. Results from stations on the island, however, do not constrain the width of the zone of anisotropy. Moreover, as shear wave splitting occurs in many regions because of a deforming asthenosphere [e.g., *Wolfe and Solomon*, 1998], such data from New Zealand might also be explained by deformation not in the lithosphere, but in the asthenosphere beneath a strong lithosphere through which the Alpine fault passes from the surface to the asthenosphere [e.g., *Klosko et al.*, 1999; *Zietlow et al.*, 2014].

With the limitations imposed by stations confined to the island and by the poor depth resolution of shear wave splitting, a network of ocean bottom seismographs (OBS) was deployed for 1 year in the region surrounding the South Island [*Collins et al.*, 2011] (Figure 1). We focus on *Pn* speeds, which complement analyses of shear wave splitting [*Zietlow et al.*, 2014] and work in progress on anisotropy of Rayleigh wave propagation. Because *Pn* propagates through the lithosphere, its anisotropy must be due to deformation of the lithosphere, not in the asthenosphere. In addition, however, the crust of New Zealand is unusually anisotropic, up to 6% in places but with different orientations [*Christensen and Okaya*, 2007]. Thus, anisotropy
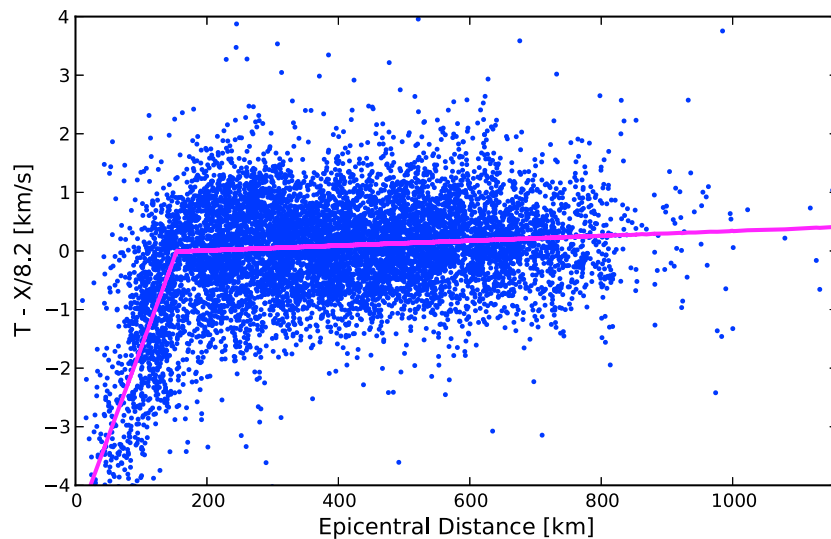
Figure 2. A total of 8950 handpicked travel times, corrected for event and station delays, plotted versus epicentral distance. The superimposed best fit travel time curves represent *Pg* and *Pn* arrivals with speeds of 6.56 km/s and 8.18 km/s, respectively. The *Pg* and *Pn* arrivals separate at 154 ± 2 km.

might contribute to shear wave splitting [*Godfrey et al.*, 2000, 2002], but even with 6% anisotropy in layers with thicknesses of 10 km [*Christensen and Okaya*, 2007], crustal anisotropy would contribute travel time anomalies of only 0.1 s. Thus, arrival times of *Pn* ought to be only weakly affected by crustal anisotropy, for most of the *Pn* paths are in the mantle and much longer.

2. Data Analysis

We examined vertical component seismograms recorded at the OBS stations, New Zealand National Seismograph Network (NZNSN) stations [*Petersen et al.*, 2011] on the South Island and at four temporary stations deployed to augment the NZNSN stations for all earthquakes reported in the NZNSN GeoNet catalog with magnitudes M_L or $m_b \geq 3.0$, events depths ≤ 50 km, and located within the region 30°S to 50°S and 164°E to 186°E. For each seismogram we examined unfiltered broadband recordings and also seismograms filtered in the frequency bands 2–10 Hz, 2–15 Hz, 3–15 Hz, 3–20 Hz, 5–15 Hz, and 5–20 Hz. We measured arrival times using different frequency bands, and we found them to be consistent when compared with neighboring bands. In most cases, we relied on the bands 2–15 Hz and 3–20 Hz, because signal-to-noise ratios were highest in these bands. We measured arrival times for all clear *P* phases (*Pg* or *Pn*). Although we measured arrival times at stations NZ02, NZ03, and NZ04 (Figure 1) and used them in preliminary analysis, we did not use them to study anisotropy, because these three stations lie on oceanic lithosphere, and our concern is anisotropy beneath continental crust. Ultimately, we used 7602 arrival times of *Pn* phases from 332 events, measured at 49 stations (Figure 1).

In a first step of analysis, we simply fit a straight line through all travel times versus epicentral distance using the locations and origin times given in either the NZNSN GeoNet (http://www.geonet.org.nz/earthquake/) catalog or the ISC catalog [*International Seismological Centre*, 2013]. Where available, we used ISC locations and origin times in preference to GeoNet values, because the ISC incorporated all of the GeoNet data. We assume that errors in locations are typically smaller than 20 km, and because we relied on earthquakes that were recorded by five or more stations, we suspect that few are mislocated by as much as 30 km. As we had measured arrival times for *Pg* phases when they were first arrivals, we discarded all arrival times at stations with short epicentral distances. Ultimately, we consider only phases with epicentral distances $\geq 1.75°$ (195 km) for paths to stations within the central part of the South Island where crust seems to be thick, and $\geq 1.5°$ (167 km) for low-lying stations and OBSs (Figure 2). We then allowed for two corrections to arrival times: (1) adjustments to origin times, but not locations, of earthquakes, and (2) station corrections. For this procedure, we considered only those earthquakes for which we had measured at least five *Pn* arrival times and only those stations where we had measured at least 10 *Pn* arrival times. Thus, for *n* events and
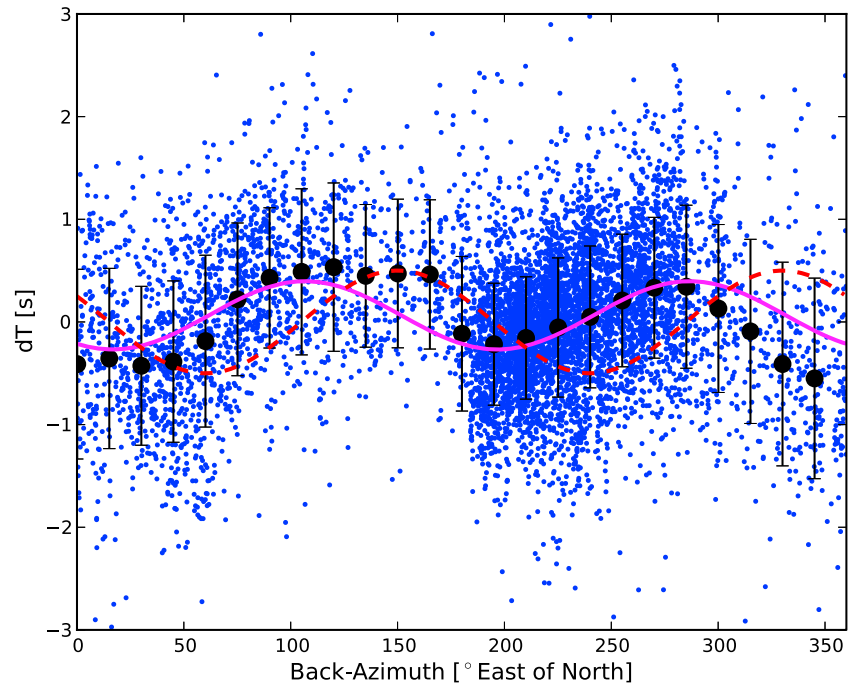
Figure 3. Plot of *Pn* travel time residuals versus back azimuth. The residuals are measured relative to the least squares, best fit straight line to all arrivals with epicentral distances greater than 1.5°. The arrival times are corrected for event and station delays, and the residuals are corrected to an epicentral distance of 400 km by multiplying by the ratio of 400 km to the epicentral distance. The magenta-colored line is the least squares best fit 2θ curve to the individual residuals. The black-filled circles show the mean residuals in bins 30° wide and overlapping by 15°. The associated vertical lines represent the ±1 sample standard deviations in each bin. The bin values are shown for guidance only. The minimum in travel time residuals at ~17° is crudely consistent with high speeds being aligned parallel to ~60°, the average relative plate motion direction for the past 20 Ma [*Cande and Stock*, 2004], but the dashed red line shows what we might expect with exact alignment.

N stations, we solved for $n + N + 2$ parameters, where the last two are the mean *Pn* speed and an average intercept time. All further analysis takes this approach of correcting arrival times for origin time corrections and station corrections, whose values we discuss below.

2.1. Sources of Scatter

Although the scatter in arrival times is not small, $\sigma = 0.8$ s, the mean speed is well defined to be 8.18 ± 0.01 km/s (Figure 2). We also fit travel times to a quadratic function of distance, but the quadratic term was too small to be resolvable. Thus, although *Pn* phases propagating to different distances might sample different depths, we could not discern any such dependence.

If anisotropy is present, it will contribute to scatter in arrival times. In a preliminary test of this, we plotted travel time residuals as a function of back azimuth (Figure 3). Two features are clear. The travel times still show large scatter, but they fit a function of the form:

$$\delta t = \delta t_0 \cos 2(\psi - \psi_0) \qquad (1)$$

which is consistent with anisotropy, and where δt is the travel time residual, ψ is the back azimuth, the azimuth from station to epicenter, δt_0 and ψ_0 are constants that we estimate. Although, even ignoring the scatter, the fit to (1) is not good, the 2ψ pattern implies that anisotropy is present. That orientation is not grossly different from what others have inferred, ~56° using *Pn* speeds at fewer stations for paths beneath the center of the island [*Bourguignon et al.*, 2007] and west of it [*Melhuish et al.*, 2005; *Scherwath et al.*, 2002], and ~20° just offshore of the east coast [*Baldock and Stern*, 2005]. This orientation also is not too different from ~55° orientations of the faster quasi-*S* wave in shear wave splitting using core phases at stations near the Alpine fault [e.g., *Duclos et al.*, 2005; *Klosko et al.*, 1999; *Savage et al.*, 2007a; *Zietlow et al.*, 2014] but mixed with nearly orthogonal orientations of ~100–140° at stations east of the East Coast

[*Zietlow et al.*, 2014]. Thus, despite the huge scatter in data in Figure 3, the residuals seem to agree that *Pn* propagates fastest in directions that are not grossly different from that of relative plate motion; because plate motion is largely strike slip, we should expect olivine crystals to be oriented so that propagation will be fastest in those directions.

Most of our effort was devoted to understanding and reducing the scatter shown in Figures 2 and 3. That work included reexamination of hundreds of seismograms with outlying arrival times, but data shown in these figures do not include observations that were discarded for whatever reasons (obvious blunders, short epicentral distances, low signal-to-noise ratios, earthquakes with location uncertainties greater than ~10 km, etc.).

A second possible source of scatter could arise from wave speeds that are not uniform across the island, either because of lateral variations in average speeds, as *Haines* [1979] inferred, or in amounts or orientations of anisotropy. The latter is especially likely, given that shear wave splitting is obviously not uniform beneath the South Island [e.g., *Duclos et al.*, 2005; *Klosko et al.*, 1999; *Savage et al.*, 2007a; *Zietlow et al.*, 2014]. Moreover, the Pacific plate underthrusts the northeastern part of the South Island, so that the uppermost mantle there is not strictly continental lithosphere. Where the Pacific plate underthrusts the North Island, it passes directly below the crust, so that along the east coast of that island, the underlying mantle lithosphere formed as Pacific plate oceanic lithosphere [e.g., *Barker et al.*, 2009; *Boyd et al.*, 2007; *Nicol et al.*, 2007; *Walcott*, 1998]. Large split times, >2 s, with fast orientations parallel to the coast characterize shear wave splitting at stations on the east coast of the North Island [*Gledhill and Gubbins*, 1996; *Gledhill and Stuart*, 1996; *Morley et al.*, 2006]. More important, *Pn* speeds along a profile parallel and beneath that east coast are extremely high, >8.7 km/s [*Chadwick*, 1997; *Eberhart-Phillips and Reyners*, 2009; *Seward et al.*, 2009]. As Pacific-plate lithosphere also underthrusts the northern end of the South Island, we might expect it to contaminate measurements, if not interpretations, of anisotropy. We attempted to account for this potential source of error by not including data for stations KHZ, NNZ, and THZ, in the northeast of the South Island, and stations, APZ, DCZ, and PYZ in the southwest of the South Island where the Australian plate underthrusts Fjordland.

Ray bending due to lateral variations in average speeds could result in our measured interstation speeds being too high. We are unable to quantify this source of error. We note, however, that *Buehler and Shearer* [2012] in their study of *Pn* arrivals recorded by USArray, where they account for the direction and curvature of the incoming wavefront, conclude that ray-bending effects do not appear to be very important.

Another obvious possible source of scatter is systematic mislocations of events, many of which lie southwest of the South Island and occurred as aftershocks of the large, $M_S = 7.8$, earthquake of 15 June 2009. Mislocations can manifest themselves in two ways. For events mislocated to the NW or SE, the differences in path lengths to stations on the South Island and assumed to lie along great circles would be shorter than the distance between the stations. For example, consider a pair of stations 200 km and 400 km from an earthquake whose epicenter is assumed to lie on a great circle between the stations. Suppose the epicenter were wrong by 20 km. Then, the back azimuths would be in error by arctan (0.1) = 5.7° and arctan (0.05) = 2.9°, and path lengths would be 201.0 km and 400.5 km. Their difference of 199.5 km differs by 0.25% from the assumed 200 km difference, a negligible amount. For northeastward or southwestward errors in locations and for earthquakes near the southwest of the island, errors in locations should affect travel times to nearby and distant stations alike, and hence not affect apparent speeds between stations. Because the data that we add are from OBSs, which have paths that are oblique to the inferred orientation of anisotropy, arrival times will be later than for paths with the same lengths to stations on the South Island, and early arrivals for paths along the island will be fit better if the epicenter is shifted northeast. Thus, the likely systematic error already present in the mislocations will be exacerbated, but the effect of anisotropy will be muted by the relocated epicenters. As our goal is to quantify magnitudes, orientations, and distributions of anisotropy, we refrained from relocating earthquakes.

As a first step toward eliminating the effect of mislocation error on scatter in residuals, we considered only differences in arrival times between pairs of stations for which paths are nearly parallel to great circles connecting such stations [*Beghoul and Barazangi*, 1989; *Haines*, 1979; *Smith and Ekstrom*, 1999]. We considered arrival time differences only for earthquakes for which the opening angle—defined as the angle between the great circle path through the two stations and the great circle path between the event
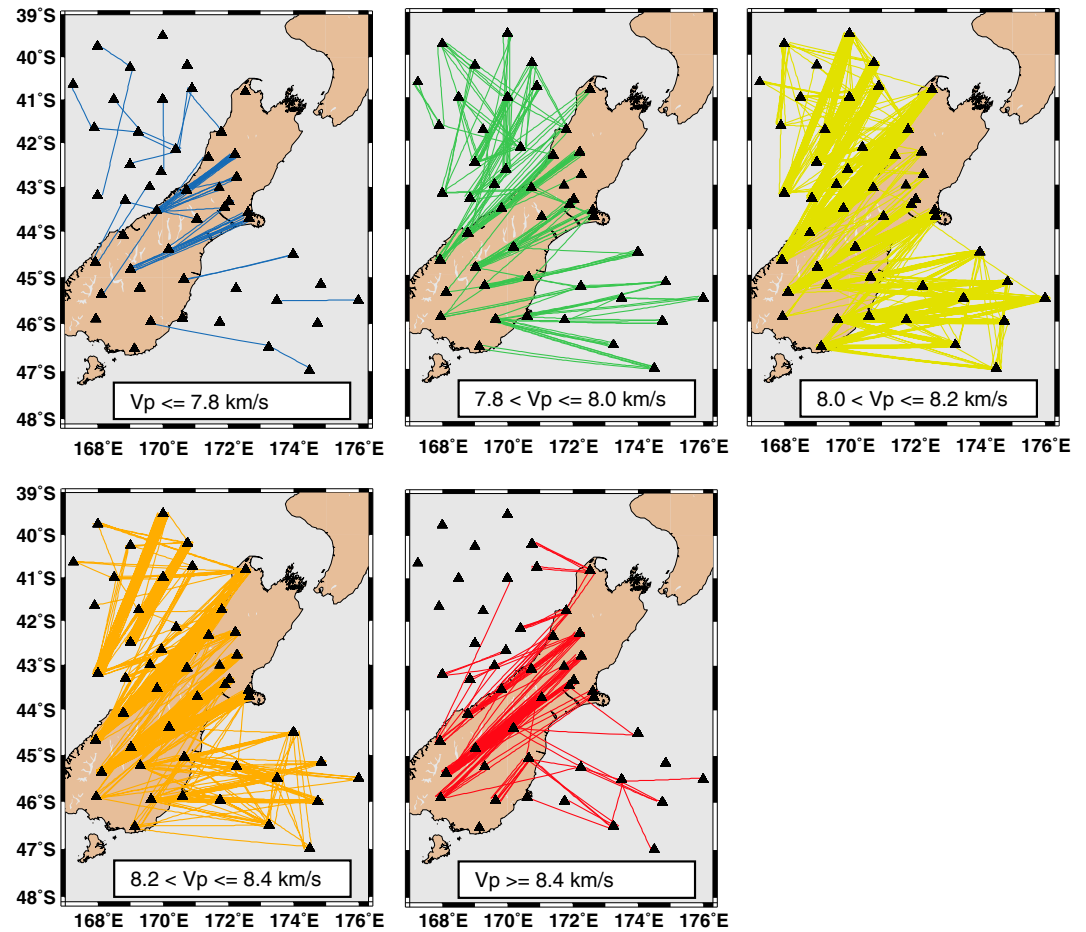
Figure 4. Maps of two-station paths showing that high speeds characterize paths that largely are aligned parallel to the island but that there remains considerable scatter.

and the farthest station—is less than 2–10°, and although inferences of anisotropy differed little, within uncertainties, for all possibilities, ultimately we settled on a maximum of only 3°. Hence, for each pair of stations we solved for

$$v_{1,2} = \frac{t_1 + \Delta t_1 - t_2 - \Delta t_2}{\Delta x_{1,2}} \tag{2}$$

where $v_{1,2}$ is the apparent speed for Pn propagation from station 2 to station 1, t_1 and t_2 are arrival times at stations 1 and 2, Δt_1 and Δt_2 are corresponding station corrections, and $\Delta x_{1,2}$ is the difference in propagation distance from the epicenter to each station.

This procedure obviously reduced the number of arrival times that we used. It also reduced scatter, but by no means all of it. For example, maps show that high speeds dominate paths between stations on the South Island and with paths roughly parallel to plate motion (~N60°E), such as between WKZ or LBZ and RPZ, FREW, OXZ, CASS, or LTZ (Figure 4). Although less clear, in part because there are fewer data, NW-SE paths that cross the South Island show low speeds. The most obvious feature shown by these maps, however, is the wide range of apparent speeds between the same pair of stations (Figure 4). For example, paths from either WKZ or LBZ to RPZ, FREW, OXZ, CASS, or LTZ, as well as those in opposite directions, include earthquakes with the full range of apparent speeds, from < 7.8 km/s to > 8.4 km/s. This can be seen by plotting Pn speeds between pairs of stations as function of the mean back azimuth from the two stations to the epicenter (Figure 5). The orientation of fastest Pn is ~56° (±3°) E, consistent with results from other studies noted above. The scatter, however, remains large, and peak-to-peak magnitude of anisotropy of ~1.9% or 0.15 km/s is notably smaller than what others have reported [*Bourguignon et al.*, 2007; *Scherwath et al.*, 2002], if not too different from the difference between 8.2 km/s parallel to the West Coast [*Melhuish et al.*, 2005]
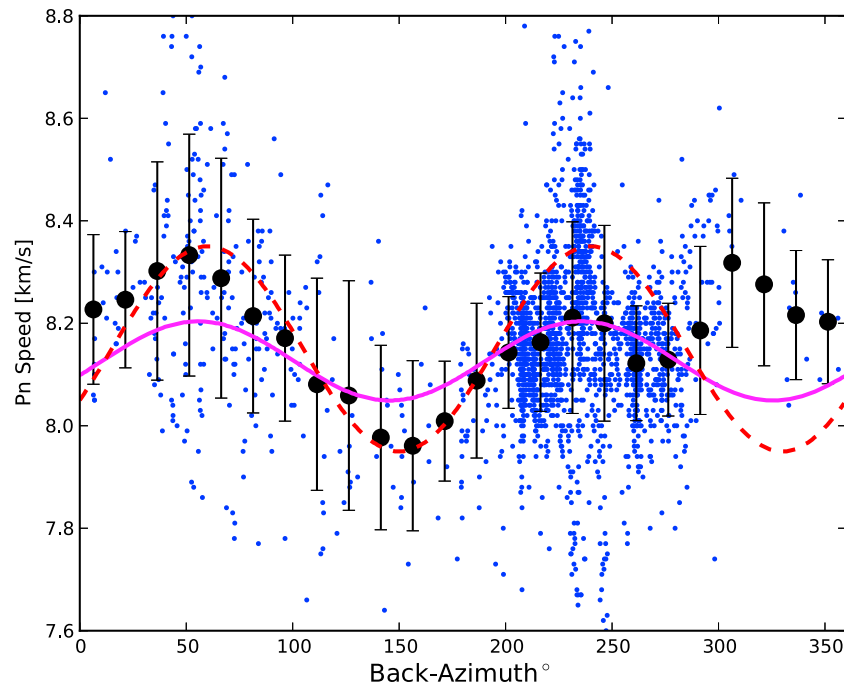
Figure 5. Plot of apparent speeds versus back azimuth using station pairs that have opening angles $\leq 3°$ and interstation distances ≥ 100 km. The magenta line is the least squares best fit 2θ curve to the individual speeds. The black-filled circles show the mean speeds in bins 30° wide and overlapping by 15°. The associated vertical lines represent the ± 1 sample standard deviations in each bin. The bin values are shown for guidance only. The direction of fastest speeds is $56° \pm 3°$. Anisotropy magnitude is 2%.

and 7.8 km/s perpendicular to it [*Van Avendonk et al.*, 2004]. We observed no dependence of apparent speed on interstation distance or on epicentral distance, which might account for some of the scatter.
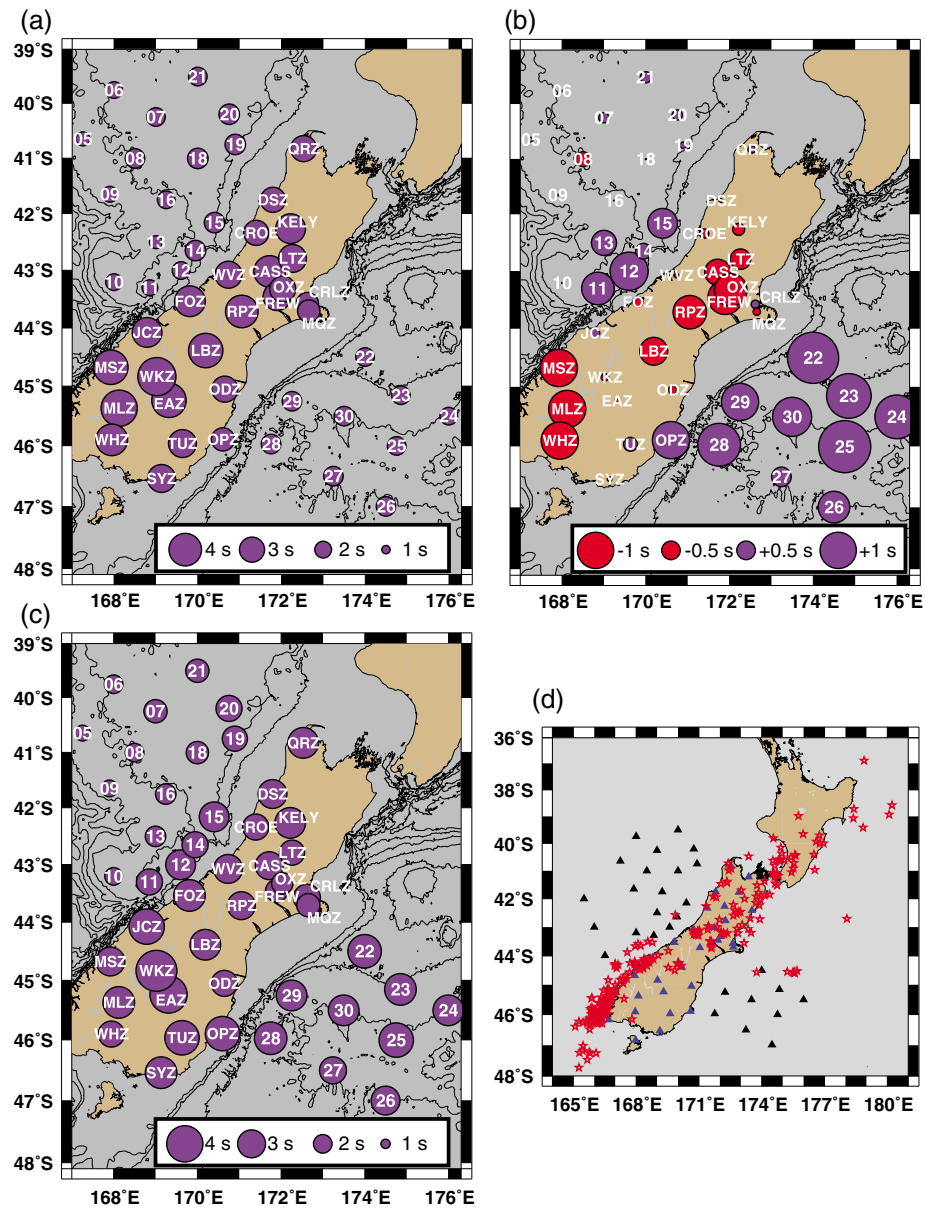
2.2. Station Corrections

As station corrections surely differ from station to station, errors in them also can contribute errors to apparent speeds. We calculated initial station delays from the crustal thickness estimates of *Salmon et al.* [2013], assuming an average crustal speed of 6.2 km/s [*Bourguignon et al.*, 2007; *Scherwath et al.*, 2003; *Van Avendonk et al.*, 2004] and an average mantle speed of 8.1 km/s (Figure 6a). We then solved for corrections to these assumed station delays by minimizing root-mean-square residuals when solving for corrections to origin times, the mean *Pn* speed, and the average intercept time (Figure 6b). Corrections (Table 1) are positive at all stations off the east coast of the island, where sediment and sedimentary rock are thick [*Uenzelmann-Neben et al.*, 2009] and exceed 1 s at NZ22 and NZ25. The adjusted station corrections range from 2 s at stations in relatively deep water northwest of the island to 4 s at stations where the crust is thickest, WKZ (Figure 6c).

For interstation distances of 100, 200, and 300 km, travel time differences are likely to be about 12.2 s, 24.4 s, and 36.6 s (for an average speed of 8.2 km/s). Thus, a plausible error of 0.1 s in station corrections (Table 1) at each of two stations, resulting in a combined error of 0.14 s in travel time differences, will contribute errors of 1.1%, 0.6%, and 0.4%, or 0.09 km/s, 0.05 km/s, and 0.03 km/s to average interstation *Pn* speeds. Clearly, expected errors in station corrections ought not to contribute much to observed scatter in residuals (Figure 2) or apparent speeds (Figure 5). Nevertheless, because they do contribute to errors in apparent speeds for short interstation distances, we limit such distances to 100 km or more.

2.3. Possible Effects of Noise on Scatter in Travel Times

For pairs of *Pn* phases, obviously one station is at least 100 km closer to the epicenter than the other, and the signal is likely to be larger at the closer station. Signals differ so much from one another that we could not use automatic picking algorithms that cross correlate signals to measure differences in arrival times. In some cases, the arrival at the closer station is emergent, and that emergent signal

Figure 6. Maps of station corrections. (a) Corrections derived from the crustal thicknesses determined by *Salmon et al.* [2013], assuming crust and mantle speeds of 6.2 km/s and 8.1 km/s, respectively. (b) Correction changes inferred from measured *Pn* arrival times and the initial corrections shown in Figure 6a. (c) Final station corrections are the sum of the values in Figures 6a and 6b. (d) Red stars show the locations of the earthquakes used to determine event and station corrections.

could be hidden at the more distant station. In such a case, the elapsed times between measured arrival times would be too large and the apparent speed too low. We have observed this phenomenon in two situations.

For a few cases where the epicentral distance to the closer station is less than ~200 km, we have seen examples where the initial arrival at the closer station is followed by a stronger signal. Such an occurrence is not obviously common, but the earlier signal might be *Pg*, not *Pn*. For this reason, we limited analysis to earthquakes whose distance to the closer of a pair of stations was ≥1.5° (167 km) and where one station is on thick crust (e.g., WKZ) to ≥1.75° (195 km).

In some cases with long epicentral distances, emergent signals at the closer station are associated with lower speeds than normal, ≤ 7.8 km/s (Figure 7). It is easy to believe that in such cases, an emergent signal

Table 1. Calculated Station Delays

Station	Event Count	Crustal Thickness (km) [Salmon et al., 2013]	Predicted Station Delay (s)	Calculated Station Delay Change (s)	Total Station Delay (s)	Standard Error of Mean (s)
CASS	40	36.5	3.79	−0.72	3.07	0.15
CRLZ	44	25.9	2.69	0.23	2.92	0.1
CROE	61	29.5	3.06	−0.25	2.81	0.09
DSZ	164	29.3	3.04	0.11	3.15	0.06
EAZ	106	39.7	4.12	−0.13	3.99	0.1
FOZ	140	36.2	3.76	−0.27	3.49	0.08
FREW	88	32.7	3.39	−0.94	2.45	0.07
JCZ	136	34.7	3.6	0.26	3.86	0.1
KELY	112	35.3	3.66	−0.33	3.33	0.07
LBZ	141	39.8	4.13	−0.75	3.38	0.07
LTZ	157	32	3.32	−0.56	2.76	0.06
MLZ	31	42.4	4.4	−1	3.4	0.12
MQZ	131	26.2	2.72	−0.21	2.51	0.07
MSZ	39	40	4.15	−1	3.15	0.1
NZ05	207	15.8	1.64	0.13	1.77	0.06
NZ06	194	19.8	2.06	−0.04	2.02	0.07
NZ07	73	22.2	2.3	0.29	2.59	0.11
NZ08	225	23.4	2.43	−0.4	2.03	0.06
NZ09	219	18.1	1.88	−0.05	1.83	0.06
NZ10	189	19.1	1.98	−0.02	1.96	0.07
NZ11	190	18.6	1.93	0.89	2.82	0.07
NZ12	106	21.5	2.23	1.03	3.26	0.08
NZ13	234	14.6	1.52	0.69	2.21	0.06
NZ14	149	23.6	2.45	0.44	2.89	0.08
NZ15	37	24.1	2.5	0.82	3.32	0.22
NZ16	253	21.5	2.23	−0.03	2.2	0.05
NZ18	250	23.5	2.44	−0.02	2.42	0.05
NZ19	239	24.6	2.55	0.18	2.73	0.04
NZ20	202	24.2	2.51	0.28	2.79	0.05
NZ21	142	22.1	2.29	0.31	2.6	0.08
NZ22	154	21.9	2.27	1.39	3.66	0.04
NZ23	123	21.6	2.24	1.23	3.47	0.06
NZ24	97	20.5	2.13	1.2	3.33	0.1
NZ25	106	21.9	2.27	1.43	3.7	0.05
NZ26	105	22.4	2.32	0.85	3.17	0.12
NZ27	181	23.2	2.41	0.54	2.95	0.08
NZ28	164	22.8	2.37	1.17	3.54	0.06
NZ29	208	22.8	2.37	1.01	3.38	0.06
NZ30	128	22.3	2.31	1.07	3.38	0.07
ODZ	197	30	3.11	−0.24	2.87	0.07
OPZ	120	27	2.8	1	3.8	0
OXZ	122	31.1	3.23	−0.88	2.35	0.06
QRZ	138	30.4	3.16	0.19	3.35	0.07
RPZ	140	37.7	3.91	−0.91	3	0.06
SYZ	172	32.3	3.35	0.14	3.49	0.08
TUZ	169	32.2	3.34	0.38	3.72	0.09
WHZ	32	37.2	3.86	−1	2.86	0.09
WKZ	78	44.7	4.64	−0.2	4.44	0.13
WVZ	137	31.3	3.25	−0.12	3.13	0.07

seen at the closer station is lost in noise at the more distant station. We also find, however, examples with emergent signals at the closer station and with high apparent speeds, ≥ 8.6 km/s; obviously, if that emergent phase were lost in noise at the more distant stations, speeds would be yet higher (Figure 8). Note that pairs of arrivals in Figures 8a and 8b for paths from WKZ to LBZ yield apparent speeds that differ little from that with propagation from LBZ to WKZ in Figure 8c.

We observed essentially all possibilities including both low and high apparent speeds with strong or emergent signals (Figures 9 and 10). The seismograms in Figures 7–10 are meant to illustrate how arrival
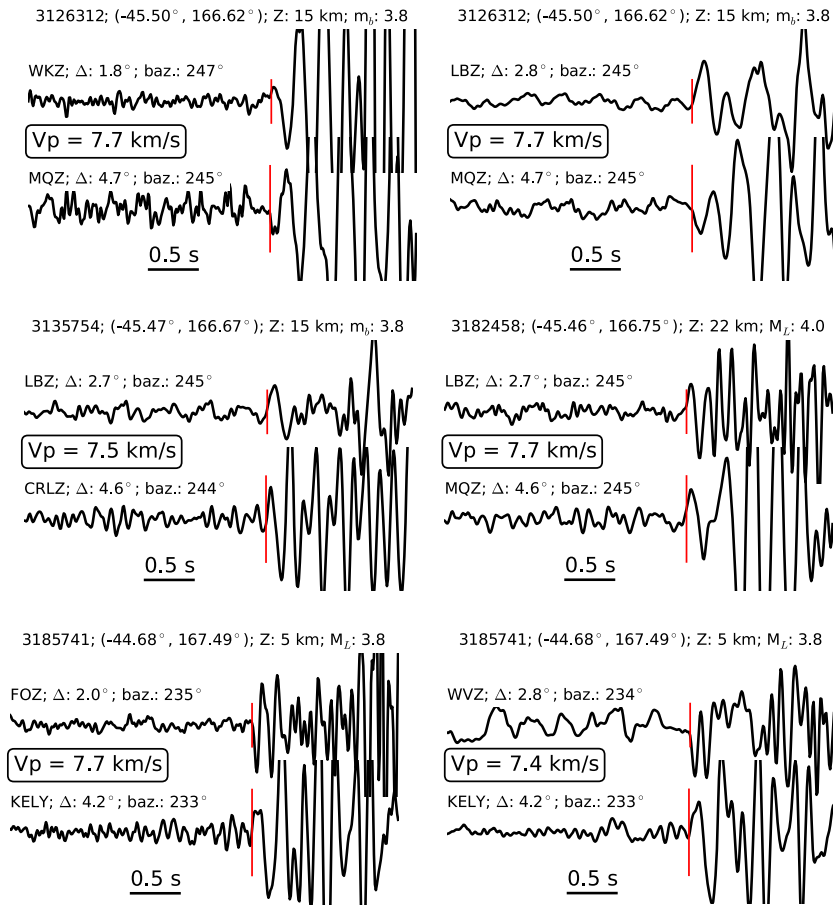
Figure 7. Examples of pairs of seismograms for along South Island paths for which the speed is low. The red vertical lines show the handpicked *Pn* arrival times.

times might have been misidentified when signal to noise ratios are not large, but we suspect that most seismologists would measure arrival times within 0.1–0.2 s of what we have picked.

Although we cannot demonstrate the following, we think that the reason for the large scatter is that we have picked late arrivals at the more distant stations. Signal-to-noise ratios at the more distant station for pairs showing low apparent speeds (Figure 7) are smaller than those for pairs of stations with high apparent speeds (Figures 9 and 10). Thus, as we discuss below, our estimates of average speeds for any azimuth may be biased toward an underestimate, but we can offer no objective quantification of such a bias. We note too that the scatter in our data is no greater, and perhaps smaller, than that in other recent studies of *Pn* anisotropy [e.g., *Buehler and Shearer*, 2014; *Shintaku et al.*, 2014].

3. Results: Distribution and Degree of Anisotropy

As we do not understand the scatter of arrival times in Figures 2–6, we lack an objective way to remove or ignore it.

The work of *Baldock and Stern* [2005], *Bourguignon et al.* [2007], and *Scherwath et al.* [2002] suggests that anisotropy is greatest beneath the South Island, with fast propagation along the axis of the island and slow propagation perpendicular to it. Thus, we divided the region into several subregions and analyzed paths within those subregions (Figure 11). For each we fit data to curves of the form

$$v = v_0 + \frac{\Delta v}{2} \cos 2(\psi - \psi_0) \tag{3}$$

where v_0 is the average speed, Δv measures the peak-to-peak anisotropy, which we measure as a percentage, $\Delta v/v_0$. Our results are summarized in Table 2. We avoid carrying out full tomographic inversion, in which
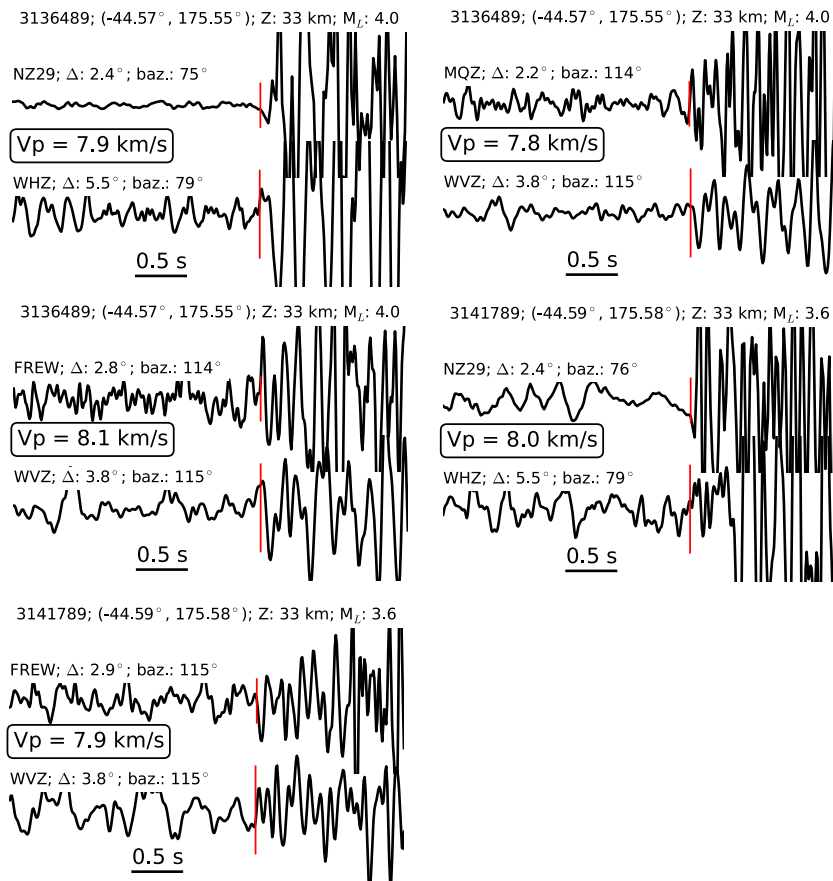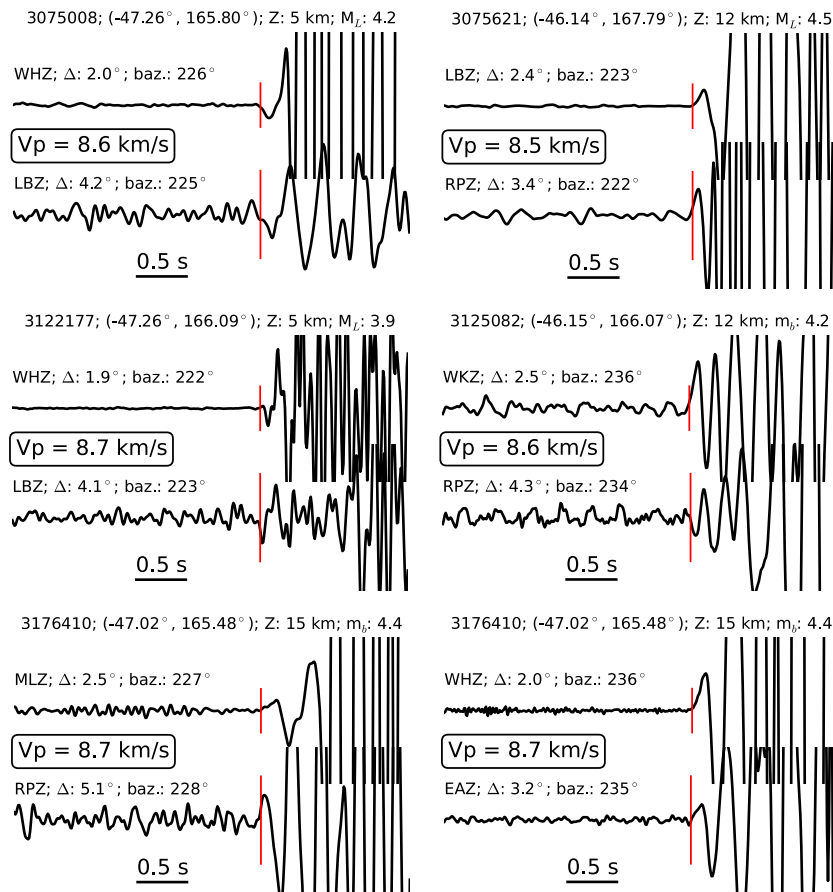
Figure 8. Examples of pairs of seismograms for across South Island paths for which the speed is low to moderate. The red vertical lines show the handpicked *Pn* arrival times.

all data are used to solve for lateral variations in mean speeds and in magnitudes and orientations of anisotropy; we anticipate that readers would not believe such results until we carry out the analysis described here. Thus, we defer tomography to future work.

Let us first consider paths largely confined to the island, including those to OBSs just west of the island (NZ10–15), but excluding the southeastern most stations (APZ, OPZ, SYZ, and TUZ) and those in the northeast (KHZ, NNZ, and THZ) that might be affected by subducted oceanic lithosphere (Figure 11). We omit the southern stations because they lie far from the most intense zone of deformation, which follows and lies east of the Alpine fault, near the West Coast. Despite the large scatter, a clear pattern emerges with fast propagation along the island (Figure 12a), with the highest speeds along paths oriented ~ N59° ± 3°E, and with a peak-to-peak amplitude of $\Delta v/v_0 = 7.9\% \pm 1.3\%$. Although we show in Figures 12–14 average speeds and their standard deviations in bins of 30° wide and overlapping by 15°, in estimating means and standard errors of speeds and azimuths, we weighted each apparent speed equally and assumed Gaussian errors. If we exclude OBSs northwest of the island and include OBS 22 and 29 southeast of the island (Figure 12b), the percent anisotropy drops to only 5.7 ± 1.3%, with a fast orientation of 34° ± 6°. By contrast, if we exclude stations on the southeast half of the island, but include OBS off the northwest coast (Figure 12c), we again measure 8.1% ± 1.0%, with a fast orientation of 60° ± 3°. Thus, the region of maximum anisotropy does not extend to the southeastern side of the island but does extend off the West Coast perhaps as much as 100 km.

Readers should note that this estimate of anisotropy might be exaggerated, for the average speed associated with it is only 7.93 km/s. The maximum speed, for paths oriented N60°E, of ~8.3 km/s is smaller than 8.5 ± 0.2 km/s, which *Bourguignon et al.* [2007] inferred from arrival times from a few earthquakes to the southwest of the island and from one northeast of their stations. As perpendicular paths are absent
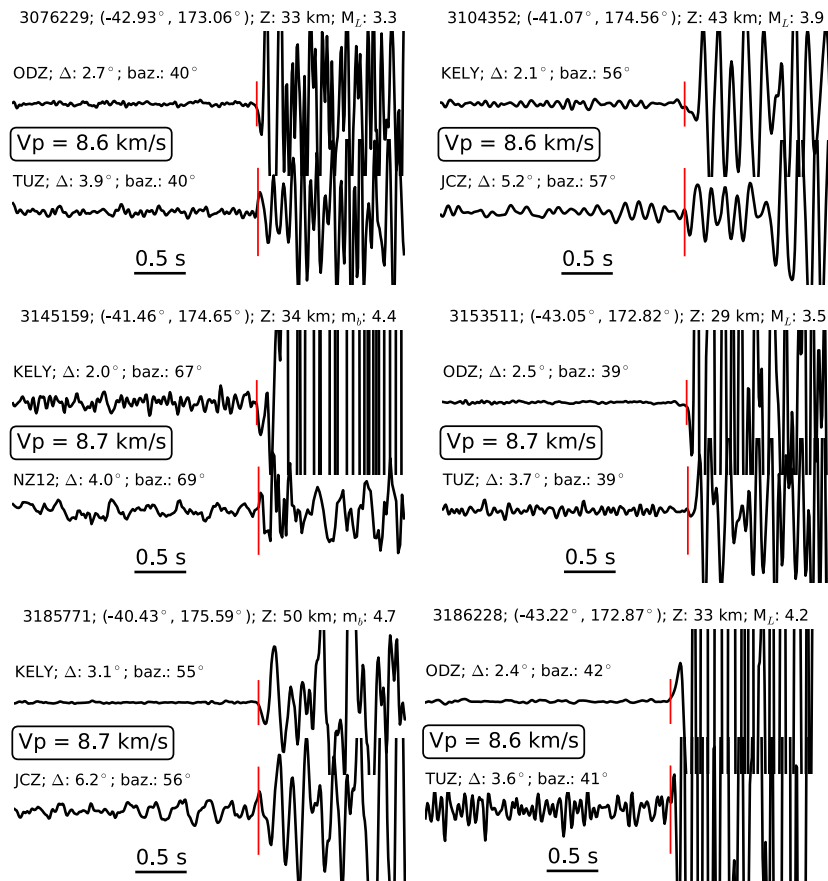
Figure 9. Examples of pairs of seismograms for South Island SW-NE paths for which the speed is high. The red vertical lines show the handpicked *Pn* arrival times.

(Figures 11a and 12), and hence no observations constrain the minimum speed, both the orientation and magnitude of anisotropy can be constrained only by paths oblique to the orientation with the fastest *Pn*, those between 080° and 120° and between 195° and 215°. Nevertheless, the marked decline in apparent speeds for back azimuths from 080° to 120° and from 215° to 195° requires anisotropy. Moreover, this estimate might underestimate anisotropy because, for reasons given above, noise would tend to bias inferred speeds toward underestimates, and the large scatter certainly permits higher speeds along the island, as observed by *Bourguignon et al.* [2007]. Using controlled sources *Scherwath et al.* [2002] measured large *Pn* anisotropy (10%) just offshore of the West Coast with fast axes approximately parallel to plate motion.

Paths confined to the OBS southeast of the island or that include stations along the southeast coast of the island show much less anisotropy than paths on the island (Figure 13). With a large gap in back azimuths between 090° and 240°, quantifying anisotropy is difficult. Using all data from the coast and offshore (Figure 13a), except for a few outliers, speeds are nearly constant at 8.17 ± 0.15 km/s or when fit to (3), 8.21 ± 0.01 km/s with a modest peak-to-peak anisotropy of $\Delta v/v_0 = 2.0\% \pm 0.3\%$. Although the calculated uncertainties suggest that anisotropy is resolved well, it clearly is small. Fast propagation is aligned N10°W ± 4°, and therefore very different from the N60°E along the island.

If we subdivide the regions sampled by paths into one that includes only the OBS (Figure 13b), the few data yield a similarly modest anisotropy: a mean speed of 8.18 ± 0.01 km/s and peak-to-peak anisotropy of $\Delta v/v_0 = 2.3\% \pm 0.5\%$. Paths for fast *Pn* are oriented at N32°W ± 5° but are less tightly constrained than when more data over a wider region are used. This modest anisotropy, if present at all, and its nearly orthogonal orientation to that beneath the island suggests that little, if any, deformation associated with Pacific-Australia plate motion reaches as far offshore as the network of OBS.

Figure 10. Examples of pairs of seismograms for South Island NE-SW paths for which the speed is high. The red vertical lines show the handpicked *Pn* arrival times.

For the region closer to shore and including paths to stations along the southeast coast and along the southeastern edge of the Southern Alps (Figure 13c), the mean speed seems a little higher, 8.31 ± 0.04 km/s, and anisotropy is greater than that for the region offshore, with a peak-to-peak range of $\Delta v / v_0 = 5.4\% \pm 0.8\%$. Fast propagation at N6°W $\pm$ 5° is rotated counterclockwise relative to that offshore (Figures 11 and 13b) but clockwise relative to that beneath the deforming part of the island (Figures 11 and 12b).
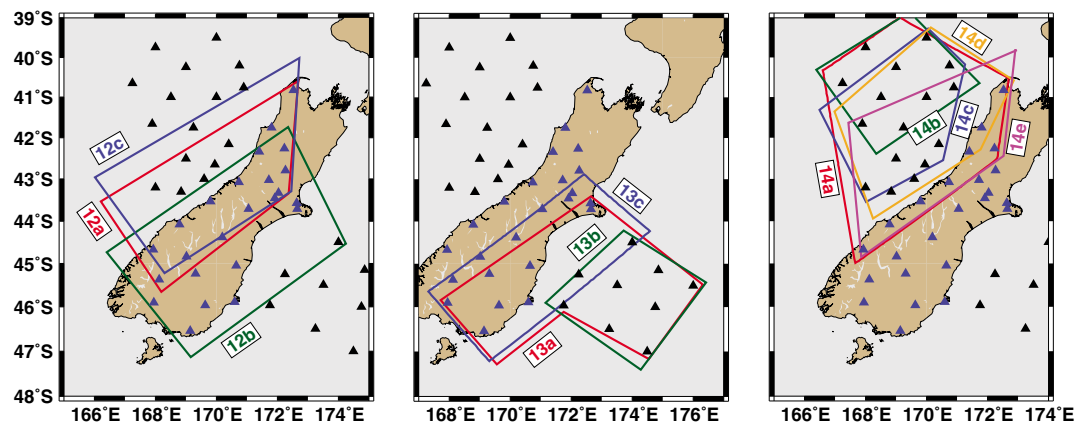
Figure 11. Maps showing regions for which we analyzed anisotropy, with labels showing figure numbers for which apparent speeds are plotted versus interstation azimuth.

Table 2. Anisotropy Measurements

| Region	Mean Distance East of Alpine Fault (km)	Half-Width (km)	Anisotropy Magnitude (%)	1σ Error in Anisotropy Magnitude (%)	Fast Axis Orientation (°E of N)	1σ Error in Fast Axis Orientation (°E of N)
Figure_12a	−24	129	7.9	1.3	58.5	3.3
Figure_12b	122	171	5.7	1.4	34.0	5.9
Figure_12c	−62	150	8.1	1.0	59.7	2.9
Figure_13a	315	201	2.0	0.3	−9.6	3.9
Figure_13b	385	135	2.3	0.5	−31.6	5.2
Figure_13c	178	115	5.4	0.8	5.9	4.7
Figure_14a	−200	240	2.0	0.3	64.6	3.6
Figure_14b	−315	139	2.5	0.8	61.3	7.4
Figure_14c	−227	154	2.8	0.4	50.2	4.2
Figure_14d	−182	163	2.1	0.3	68.4	3.9
Figure_14e	−127	141	3.5	0.5	64.2	3.8

The different orientation of fast propagation for the region along the east coast of the South Island, N32°W, from that along the Southern Alps, N60°E suggests that deformation associated with the building of the Alps has had little effect on the region to the southeast. It is possible that there is a preexisting fabric, such as that hinted by the data from offshore (Figure 13b) and by S wave splitting measurements using core phases from the OBS [*Zietlow et al.*, 2014]. Moreover, S wave splitting measurements from stations near TUZ and ODZ [*Klosko et al.*, 1999] and also at SYZ and ODZ (Figure 1) [*Zietlow et al.*, 2014] show fast polarizations of quasi-S waves of ~ N20°W. In any case, it seems clear that if deformation of the southeast margin of the South Island and offshore has occurred during the shearing of the South Island in Cenozoic time, the amount of right lateral shearing aligned at N60°E must be much smaller, by 10 times or more, than that beneath the deformed part of the South Island.

Paths confined to the OBS northwest of the island or that include stations along the northwest coast of the island show modest anisotropy (Figure 14), but with an alignment more similar to that beneath the island than the results southeast of the island (Figure 12). When the entire region spanned by the OBS offshore and stations within the Southern Alps are considered, there is a large scatter with a suggestion of anisotropy (Figure 14a): a mean speed of 8.11 ± 0.01 km/s, and a modest peak-to-peak anisotropy of $\Delta v/v_0 = 2.0\% \pm 0.3\%$.

For the westernmost part of the OBS network, data are few, but anisotropy must be small (Figures 11 and 14b): $\Delta v/v_0 = 2.3\% \pm 0.6\%$, and fast propagation is oriented N59°E ± 5°. Similarly, for paths between central OBS off the west coast (Figures 11 and 14c–14e), the azimuthal range sampled is small, but anisotropy must be small: $\Delta v/v_0 = 2.8\% \pm 0.4\%$, 2.1% ± 0.3%, or 3.5% ± 0.5%. For all of these subregions, however, orientations of fast propagation are in the range N50–70°E, not very different from that farther east.

To examine these results further, we plot in Figure 15 both peak-to-peak magnitudes of anisotropy and orientations of fast propagation versus the distance from the Alpine Fault to the centroids of our subnetworks (Figure 11). The largest peak-to-peak range of speeds are for paths confined along the northwest side of the South Island and parallel to that coast between OBS offshore of it (Figure 12), and the orientation, N60°E, is essentially parallel to the Southern Alps and to relative plate motion. The orientation for subregions to the northwest is similar, but the amount decreases systematically and sharply (Figures 11, 12c, and 15). The very different orientations for the region to the southeast deny the amounts of anisotropy there a straightforward interpretation, but again the smaller amounts suggest that the anisotropy associated with strain along the island does not extend much more than 100 km southeast of the Southern Alps.

In Figure 16, we plot *Pn* anisotropy at the centroids of our subnetworks and compare *Pn* orientations and magnitudes with S wave splitting measurements made using core phases [*Zietlow et al.*, 2014]. Although the parameters that describe *P* and *S* wave anisotropy are not the same, we note that for the region to the southeast, both measurements show a reorientation of fast azimuths from the northwest to a direction parallel to the Alpine Fault. West of the Alpine Fault, the anticlockwise shift evident in the S wave measurements is not seen in our *Pn* measurements.
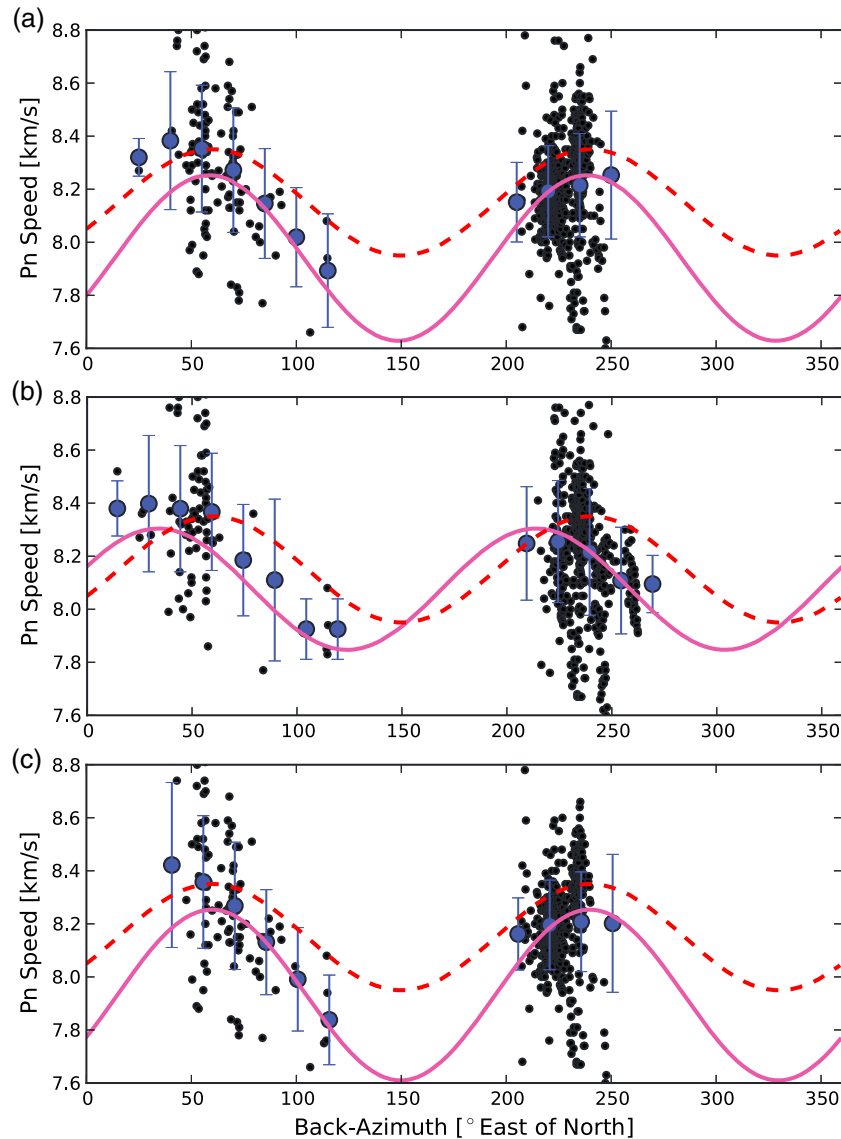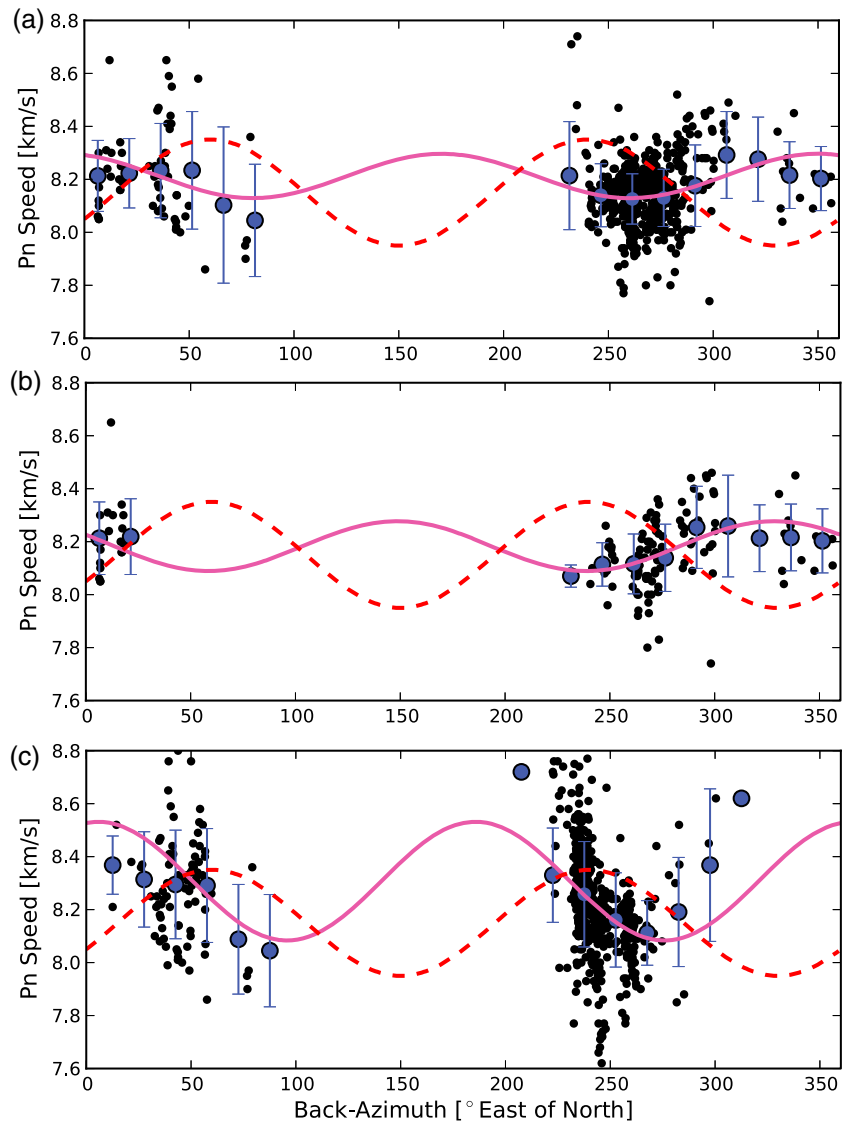
Figure 12. Plots of speeds versus azimuth between stations for paths largely confined to the island (see Figure 11): (a) using nearly all stations on the island, plus NZ10–15; (b) using stations from the central part of the island plus NZ22 and NZ29 but not stations on the West Coast; (c) using stations on the northwest side of the island, plus NZ10–16. For all plots, some stations at the southwest end (APZ and PYZ) and at the north end (KHZ, THZ, and NNZ) of the South Island were not used. The magenta-colored line is the least squares best fit 2θ curve to the individual speeds. The black-filled circles show the mean residuals in bins 30° wide and overlapping by 15°. The associated vertical lines represent the ±1 sample standard deviations in each bin. The bin values are shown for guidance only. The red dashed line shows the predicted fit if the fastest speeds were aligned parallel to 60°, the average relative plate motion direction for the past 20 Ma [*Cande and Stock*, 2004].

4. Interpretations

The results described above bear on two aspects of anisotropy: the mechanism by which the uppermost mantle becomes anisotropic and the processes responsible for the deformation of the mantle. Before discussing these aspects, let us consider some background facts.

4.1. Relationships of Anisotropy to Crystal Deformation and Alignment

Olivine is the dominant mineral of the upper mantle, and it is especially anisotropic. Thus, we follow tradition and assume that alignment of olivine crystals is responsible for the anisotropy that we have measured.
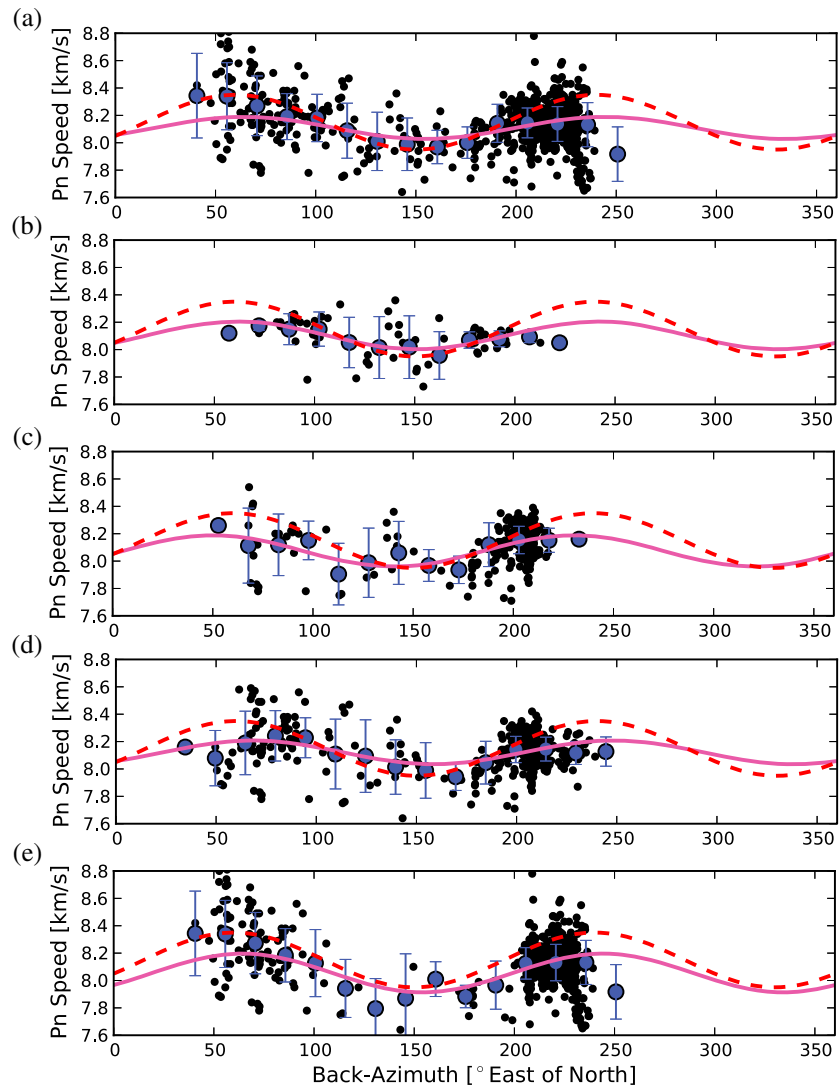
Figure 13. Plots of speeds versus azimuth between stations for paths to OBS southeast of the island (Figure 11): (a) all paths between stations offshore (NZ22–NZ30) and along the southeast coast (CRLZ, EAZ, MQZ, ODZ, OPZ, SYZ, TUZ, and WHZ); (b) only OBS (NZ22–NZ30) and therefore far offshore; (c) the onshore stations in Figure 13a plus six inland stations (FREW, LBZ, MLZ, OXZ, RPZ, and WKZ) and two offshore stations (NZ22 and NZ29). Curves are as described in the caption to Figure 12.

Most laboratory studies of olivine have been carried out at temperatures typical of the base of the lithosphere or top of the asthenosphere, 1200–1300°C [e.g., *Karato et al.*, 2008], and field observations have typically considered samples deformed at such temperatures [e.g., *Nicolas et al.*, 1973; *Warren et al.*, 2008]. At small strains, olivine deforms so that *P* and *S* waves should travel fastest when *P* propagates parallel to the axis of maximum elongation, and *S* is polarized parallel to maximum elongation [e.g., *McKenzie*, 1979; *Ribe*, 1992; *Ribe and Yu*, 1991; *Vauchez et al.*, 2012]. In a regime of simple shear, the orientation of maximum elongation will initially, at infinitesimal strain, be oriented at 45° to the plane of shear, and then as strains increase becomes parallel to the direction of relative displacement in the plane of shear.

In addition to deforming and rotating, however, olivine crystals also realign during dynamic recrystallization. *Zhang and Karato* [1995] showed in experiments at 1300°C that when strains exceed approximately unity in simple shear, the olivine crystals align as if an infinite strain had developed, but for only 1200°C, greater strain was required to cause such alignment. *Bystricky et al.* [2000] obtained results similar to those of

Figure 14. Plots of speeds versus azimuth between stations for paths to OBS northwest of the island (Figure 11): (a) all paths between stations offshore (NZ05–NZ21) and along the northwestern side of the island (CASS, CROE, KELY, DCZ, DSZ, FOZ, JCZ, MSZ, PYZ, and WVZ); (b) only OBS far offshore (NZ05–NZ09 and NZ16–NZ21); (c) all OBS off the west coast except NZ05, NZ06, NZ11, and NZ12; (d) all OBS off the west coast except NZ05 and NZ06, but with stations on the northwestern Coast (CROE, DSZ, and QRZ); (e) only OBS close to the west coast (NZ09–NZ19) plus those along the coast (CROE, KELY, DSZ, FOZ, JCZ, MSZ, QRZ, and WVZ). Curves are as described in the caption to Figure 12.

Zhang and Karato [1995] in experiments carried out at higher stresses but at the same temperatures. Field observations of olivine deformed at comparable temperatures, made by *Warren et al.* [2008], corroborate such an alignment at high strain. Further experiments showed that in the presence of abundant hydrogen ("water"), olivine can deform differently, so that orientations of fast and slow *P* and quasi-*S* propagation differ by as much as 90° from those at low hydrogen concentrations [*Jung and Karato*, 2001; *Jung et al.*, 2006; *Katayama et al.*, 2004]. Consensus holds, however, that these results do not bear on lithospheric deformation [e.g., *Vauchez et al.*, 2012].
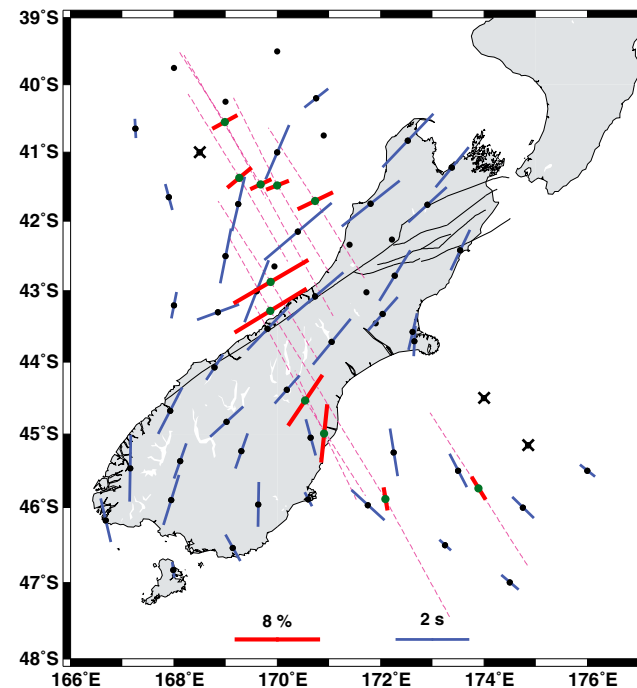
Where dynamic recrystallization does not play an important role, *P* waves should propagate fastest parallel to the orientation of maximum elongation, with the magnitude of anisotropy proportional to the amount of strain. Far from a region undergoing strike-slip shear, anisotropy should be negligible or inherited from an earlier phase of deformation. Closer to the region of maximum strain, the orientation should decrease gradually from 45° to the trend of the shear zone toward parallel to that trend [e.g., *Ribe*, 1992].
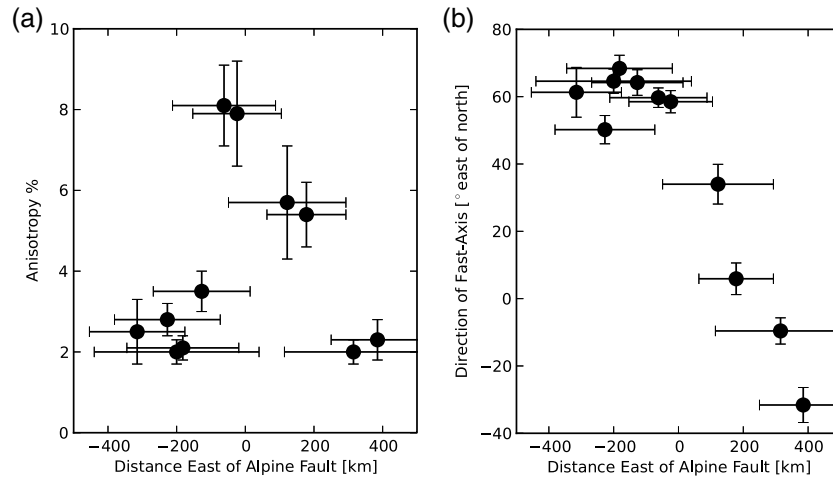
Figure 15. (a) Peak-to-peak ranges of speeds and (b) orientations of fast propagation versus distance from the Alpine Fault to the centroids of the subnetworks shown in Figure 11. Vertical error bars show 1σ estimates, and horizontal error bars define the widths of the regions sampled.
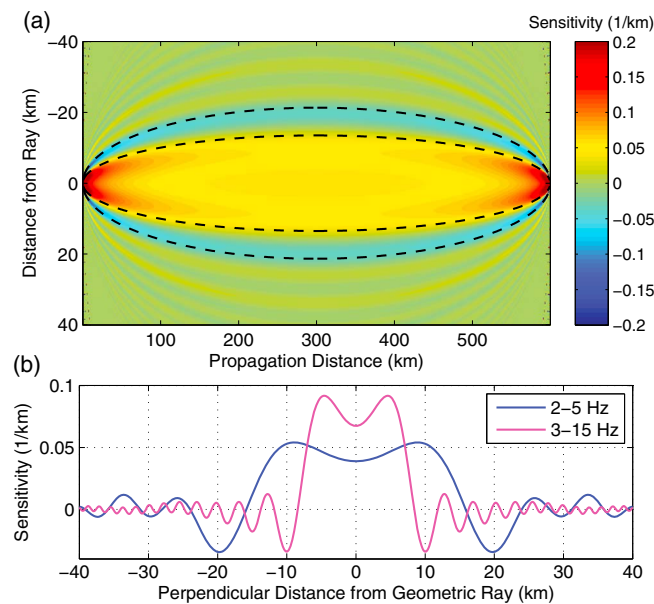
4.2. Temperatures in the Mantle Beneath New Zealand

Temperatures in the mantle where *Pn* propagates are likely to be low, at least compared to those of both relevant laboratory measurements and where anisotropy that contributes to shear wave splitting lies. *Pn* travels in the uppermost mantle, and in the New Zealand region, crust is relatively thin, with thicknesses of

only ~20 km offshore, ~27 km along the coastlines, and reaching a maximum of ~45 km [*Godfrey et al.*, 2001; *Melhuish et al.*, 2005; *Salmon et al.*, 2013; *Scherwath et al.*, 2003; *Van Avendonk et al.*, 2004]. Measurements of heat flux through the crust of New Zealand are few, and where not perturbed by rapid erosion or by fluids [e.g., *Townend*, 1999], they are typical of continental crust, ~60 mW/m^2 [*Funnell et al.*, 1996; *Godfrey et al.*, 2001; *Pandey*, 1981]. For such conditions, temperatures at the Moho could reach 600°C beneath the thickest crust, but in general they should be colder [e.g., *Pandey*, 1981; *Shi et al.*, 1996]. Consistent with this range, the presence of subcrustal seismicity beneath the South Island [e.g., *Boese et al.*, 2013; *Kohler and Eberhart-Phillips*, 2003; *Reyners*, 1987, 2005] suggests that temperatures at depths of 50–100 km are less than 600–800°C [e.g., *Chen and Molnar*, 1983; *McKenzie et al.*, 2005].

The *Pn* phase propagates as a wave rather than a zero thickness ray and as such samples a finite thickness of the upper mantle rather than an infinitesimally thin region just below the Moho. To estimate the depth extent of

Figure 16. Magnitude and orientation of *Pn* anisotropy (red bars) plotted at the centroids of the subnetworks shown in Figure 11. The *Pn* measurements represent averages over these subnetworks, and the widths of these regions perpendicular to the trend of the Alpine Fault are indicated by the magenta dashed lines. (The trends of the dashed lines are adjusted slightly to avoid overlap.) Also shown are the SKS splitting measurements (blue bars) of *Zietlow et al.* [2014]. The thick black lines show the Alpine Fault and the Marlborough Fault System to its north [*Litchfield et al.*, 2014].

(a)

(b)

Figure 17. (a) Two-dimensional, finite frequency, travel time delay Fréchet kernels for a transmitted *P* wave [*Spetzler and Snieder*, 2001, 2004]. Medium has a uniform speed of 8.1 km/s, and the kernel is calculated for the frequency band 2–5 Hz. The dashed black lines represent the first Fresnel zones for rays of frequency 2 Hz and 5 Hz. (b) Cross sections at a range of 300 km of the Fréchet kernels for waves of frequency 2–5 Hz and 3–15 Hz.

the region to which the *Pn* phase is sensitive, we calculated finite frequency Fréchet sensitivity kernels using the two-dimensional formulation of *Spetzler and Snieder* [2001, 2004]. The depth extent of the region of sensitivity increases with decreasing frequency and increasing propagation distance. Figure 17a shows the sensitivity kernel for a 2–5 Hz wave propagating over a distance of 600 km, a "worst case scenario" for our experiment. Recall that we see no resolvable variations in *Pn* speed with epicentral distance (Figure 2), suggesting a small or zero velocity gradient in the mantle. The region of sensitivity in Figure 17 extends ± ~20 km on either side of the nominal ray path. Extrapolating this to our experiment suggests that the *Pn* phases that we measure sample at most the uppermost 20 km of the mantle. Assuming a range of temperature gradients of 5–10°C/km and Moho temperatures of 500–600°C, the temperature of the mantle

sampled by *Pn* is less than 600–800°C and most likely closer to the low-temperature bound of 500°C than the upper bound.

Interpreting *Pn* speeds, where *Pn* propagates through mantle at temperatures lower than ~800°C, and possibly lower than 600°C, using experiments carried out at temperatures of 1200–1300°C, obviously carries some risk. The stresses deforming olivine at 600–800°C will be much higher than those at 1200–1300°C, and high and low shear stress might deform olivine differently. The similarity of the results of *Bystricky et al.* [2000], carried out at relatively high stress, to those of *Zhang and Karato* [1995] offers weak justification for assuming that *P* waves propagate fastest in directions parallel to strikes of strike-slip shear zones where strain is large. Yet because *Bystricky et al.* [2000] also observed dynamic recrystallization, the similar orientations of fast *Pn* propagation and relative plate motion raise the surprising possibility that dynamic recrystallization occurs at temperatures as low as 600°C. Moreover, for such a low temperature range, Peierls creep, not dislocation creep, seems necessary [e.g., *Demouchy et al.*, 2009; *Evans and Goetze*, 1979; *Mei et al.*, 2010; *Raterron et al.*, 2004].

4.3. Plausible Strain Field Across New Zealand

The measurements of *Pn* anisotropy show fast propagation aligned essentially parallel to the average direction of relative plate motion since 20 Ma. We cannot define the width of the zone of large anisotropy precisely, but large magnitudes of anisotropy, ~8%, characterize a zone perhaps as wide as 100 to 200 km, and in general much lower amounts typify the flanking regions.

We may ask the question: would strain in the absence of dynamic crystallization be sufficient to align olivine crystals so that fast propagation was indistinguishable from being parallel to relative plate motion? The angle ϑ between the orientation of maximum elongation and the strike of the shear zone is given by

$$\tan 2\vartheta = \frac{2W}{D} \qquad (4)$$

where W is the width of the shear zone, and D is the total displacement [e.g., *Molnar et al.*, 1999]. For $W = 100$ or 200 km, $\vartheta = 6.6°$ or 12.6°. Although both are larger than 1σ uncertainties in orientations of fast

propagation, the simplifying assumptions made here surely allow for $\vartheta = 6.6°$ to be indistinguishable from $\vartheta = 0°$, and perhaps also for $\vartheta = 12.6°$. So, although the results presented here suggest that dynamic recrystallization may have played a role in Pn anisotropy, we refrain from drawing such a conclusion and merely raise it as a possibility.

4.4. Relationship of Anisotropy to Continental Deformation

A thin viscous sheet in a gravity field provides a simple approximation for large-scale deformation of continuously deforming lithosphere [e.g., *Bird and Piper*, 1980; *England and McKenzie*, 1982, 1983]. The basic assumption is that deformation does not vary vertically, so that integrating the 3-D equation of equilibrium yields two equations that describe the two horizontal components of velocity.

England et al. [1985] derived a scaling relationship for the dependence of velocity and strain from the boundary of a thin viscous sheet that deforms in response to an imposed velocity on a portion of the sheet. They showed that components of velocity and strain rate should decay approximately exponentially, $\exp(-|x|/x_0)$, where x is the distance from the edge of the thin viscous sheet, and x_0 is a characteristic distance. For deformation obeying a power law relationship of the form, $\dot{\varepsilon} \sim \tau^n$, where $\dot{\varepsilon}$ is typical strain rate and τ is the relevant deviatoric stress, and for a strike-slip boundary condition on which a y component of velocity is imposed over a distance L, they found that

$$x_0 = \frac{L}{4\pi\sqrt{n}} \tag{5}$$

England et al. [1985] and *Dayem et al*. [2009] corroborated this result with numerical experiments.

The model used by *England et al*. [1985], however, assumed a rigid flank to the deforming sheet, and for New Zealand, deformation presumably occurs over a finite width that decays into lithosphere on both of the adjacent sides. In the simplest extension of their work, we simply assume the same exponential decrease into both sides. Moreover, if we assume that the width of straining of W corresponds to the region between $-2x_0$ and $+2x_0$, then $x_0 = W/4$. For values of $W = 100$ or 200 km, for $n = 3$, (5) would correspond to a length of the boundary of ~550 or 1100 km, which resemble those inferred by *Zietlow et al*. [2014] from the distribution of shear wave splitting. If Peierls creep occurred, however, then $n \approx 10$ [e.g., *Dayem et al*., 2009], and $x_0 = 50$ km or 100 km would translate into lengths of the boundary of $L \approx 1000$ or 2000 km. This inference, however, should be tempered by numerical experiments by *Sonder and England* [1986] that showed that a thin layer at the top of a thin viscous sheet would not affect its average properties strongly. In any case, values of $W = 100$ km or 200 km crudely fit the approximately 1000 km long plate boundary along the South Island, with the smaller value of W more consistent with Peierls creep.

5. Conclusions

With the goal of measuring amounts of anisotropy and the orientations of the fastest Pn phases, we measured 7602 Pn arrival times from 332 regional earthquakes at both stations of the New Zealand National Network and Ocean Bottom Seismographs that we deployed surrounding the island [e.g., *Collins et al*., 2011]. Using these arrival times and hypocenters given by the New Zealand National Seismograph Network and the International Seismological Centre, we solved for corrections to origin times of earthquakes and station delays at the various stations. Because of large scatter in arrival times that we could not account for, we exploited travel time differences at stations at least 100 km apart and with opening angles to earthquake epicenters of less than 3°. This approach removed contributions of errors in hypocenters and origin times and in Pn speeds between earthquakes and the nearer stations. Despite remaining scatter, clear differences in average Pn speeds between stations demonstrate anisotropy of ~8% beneath the South Island, with the fastest Pn phases propagating N60°E ± 3°, or N120°W. This orientation matches the N60°E (N120°W) 20 Ma average orientation of the relative plate motion between the Pacific and Australian plates, which has been accommodated largely by right lateral shear [e.g., *Cande and Stock*, 2004]. Thus, this anisotropy surely results from shear of the lithosphere associated with the relative displacement of the plates.

Paths traversing the region southeast of the South Island and including onshore parts of the island show a somewhat smaller magnitude of anisotropy, ~2 ± 0.4%, but with a very different orientation of fast propagation: between north-south and N30°W. This orientation nearly orthogonal to that along deforming

region of the South Island suggests that it owes its existence to deformation that predates Cenozoic relative plate motion. On the northwest side of the island, anisotropy also becomes small (~2%).

These results suggest localized deformation along a zone ~100–200 km wide. Given the 850 km of relative plate motion, for different parameterizations of the distribution of strain (constant or decaying exponentially with distance from a zone of maximum shear), the magnitude of simple shear strain, γ (= displacement divided by width of deforming zone) ranges from ~4 to ~8. If olivine crystals have become aligned in a zone of simple shear, this range of values would call for orientations of maximum elongation rotated counterclockwise by ~6° to 13°, relative to the N60°E ($\pm \sim 5°$) orientation of relative plate motion. Thus, the ~ N60°E orientation of fast *Pn* propagation is consistent with finite simple shear but also raises the possibility that dynamic recrystallization has occurred [e.g., *Bystricky et al.*, 2000; *Zhang and Karato*, 1995]. The low temperatures, ≤ 500–800°C, likely to characterize the depths where *Pn* propagates, suggest that Peierls creep, not dislocation creep should operate, but such low temperatures surely also cast doubt on any inference of dynamic recrystallization in the depth range sampled by *Pn*.

We applied the simple scaling law, equation (5) above, that *England et al.* [1985] proposed for a thin viscous sheet deformed by strike-slip shear along a boundary of finite length. Applying (5), assuming that $n \approx 3$–10 in the constitutive law relating stress to strain rate, and using a 100 or 200 km width of the deforming zone that we infer from *Pn* anisotropy yields an ~500 to 2000 km along-strike length of the boundary. The approximate agreement with the length of boundary along the South Island supports the application of a thin viscous sheet to continental deformation.

References

Baldock, G., and T. Stern (2005), Width of mantle deformation across a continental transform: Evidence from upper mantle (*Pn*) seismic anisotropy measurements, *Geology*, 33, 741–744.

Barker, D. H. N., R. Sutherland, S. Henrys, and S. Bannister (2009), Geometry of the Hikurangi subduction thrust and upper plate, North Island, New Zealand, *Geochem. Geophys. Geosyst.*, 10, Q02007, doi:10.1029/2008GC002153.

Beavan, J., et al. (1999), Crustal deformation during 1994–1998 due to oblique continental collision in the central Southern Alps, New Zealand, and implications for seismic potential of the Alpine fault, *J. Geophys. Res.*, 104, 25,233–25,255, doi:10.1029/1999JB900198.

Beghoul, N., and M. Barazangi (1989), Mapping high *Pn* velocity beneath the Colorado Plateau constrains uplift models, *J. Geophys. Res.*, 94, 7083–7104, doi:10.1029/JB094iB06p07083.

Bird, P., and K. Piper (1980), Plane stress finite element models of tectonic flow in southern California, *Phys. Earth Planet. Int.*, 21, 58–175.

Boese, C. M., T. A. Stern, J. Townend, S. Bourguignon, A. Sheehan, and E. G. C. Smith (2013), Sub-crustal earthquakes within the Australia-Pacific plate boundary zone beneath the Southern Alps, New Zealand, *Earth Planet. Sci. Lett.*, 376, 212–219.

Bourguignon, S., T. A. Stern, and M. K. Savage (2007), Crust and mantle thickening beneath the southern portion of the Southern Alps, New Zealand, *Geophys. J. Int.*, 168, 681–690.

Boyd, O. S., M. K. Savage, A. F. Sheehan, and C. H. Jones (2007), Illuminating the plate interface structure beneath Cook Strait, New Zealand, with receiver functions, *J. Geophys. Res.*, 112, B06310, doi:10.1029/2006JB004552.

Buehler, J. S., and P. M. Shearer (2012), Localized imaging of the uppermost mantle with USArray *Pn* data, *J. Geophys. Res.*, 117, B09305, doi:10.1029/2012JB009433,

Buehler, J. S., and P. M. Shearer (2014), Anisotropy and *Vp/Vs* in the uppermost mantle beneath the western United States from joint analysis of *Pn* and *Sn* phases, *J. Geophys. Res. Solid Earth*, 119, 1200–1219, doi:10.1002/2013JB010559.

Bystricky, M., K. Kunze, L. Burlini, and J.-P. Burg (2000), High shear strain of olivine aggregates: Rheological and seismic consequences, *Science*, 290, 1564–1566.

Cande, S. C., and J. M. Stock (2004), Pacific-Antarctic-Australia motion and the formation of the Macquarie Plate, *Geophys. J. Int.*, 157, 399–414.

Chadwick, M. P. (1997), The 1991 Hikurangi margin seismic refraction experiment, PhD thesis, 234 pp., Victoria Univ. of Wellington, Wellington, New Zealand.

Chen, W.-P., and P. Molnar (1983), Focal depths of intracontinental and intraplate earthquakes and their implications for the thermal and mechanical properties of the lithosphere, *J. Geophys. Res.*, 88, 4183–4214, doi:10.1029/JB088iB05p04183.

Christensen, N. I., and D. A. Okaya (2007), Compressional and shear wave velocities in South Island New Zealand rocks and their application to the interpretation of seismological models of the New Zealand crust, in *A Continental Plate Boundary: Tectonics at South Island, New Zealand*, *Geophys. Monogr.*, vol. 175, edited by D. Okaya, T. Stern, and F. Davey, pp. 115–155, AGU, Washington, D. C.

Collins, J. A., P. Molnar, and A. F. Sheehan (2011), Multibeam bathymetric surveys of submarine volcanoes and mega-pockmarks on the Chatham Rise, New Zealand, *N. Z. J. Geol. Geophys.*, 54, 329–339.

Dayem, K. E., G. A. Houseman, and P. Molnar (2009), Localization of shear along a lithospheric strength discontinuity: Application of a continuous deformation model to the boundary between Tibet and the Tarim Basin, *Tectonics*, 28, TC3002, doi:10.1029/2008TC002264.

Demouchy, S., S. E. Schneider, S. J. Mackwell, M. E. Zimmerman, and D. L. Kohlstedt (2009), Experimental deformation of olivine single crystals at lithospheric temperatures, *Geophys. Res. Lett.*, 36, L04304, doi:10.1029/2008GL036611.

Duclos, M., M. K. Savage, A. Tommasi, and K. R. Gledhill (2005), Mantle tectonics beneath New Zealand inferred from SKS splitting and petrophysics, *Geophys. J. Int.*, 163, 760–774.

Eberhart-Phillips, D., and M. Reyners (2009), Three-dimensional distribution of seismic anisotropy in the Hikurangi subduction zone beneath the central North Island, New Zealand, *J. Geophys. Res.*, 114, B06301, doi:10.1029/2008JB005947.

England, P., and D. McKenzie (1982), A thin viscous sheet model for continental deformation, *Geophys. J. R. Astron. Soc.*, 70, 295–321.

England, P., and D. McKenzie (1983), Correction to: A thin viscous sheet model for continental deformation, *Geophys. J. R. Astron. Soc.*, *73*, 523–532.

England, P. C., G. A. Houseman, and L. Sonder (1985), Length scales for continental deformation in convergent, divergent, and strike-slip environments: Analytical and approximate solutions for a thin viscous sheet model, *J. Geophys. Res.*, *90*, 523–532.

Evans, B., and C. Goetze (1979), The temperature variation of hardness of olivine and its implication for polycrystalline yield stress, *J. Geophys. Res.*, *84*, 5505–5524, doi:10.1029/JB084iB10p05505.

Funnell, R. H., D. S. Chapman, R. G. Allis, and P. A. Armstrong (1996), Thermal state of the Taranaki Basin, New Zealand, *J. Geophys. Res.*, *101*, 25,197–25,215, doi:10.1029/96JB01341.

Gledhill, K., and D. Gubbins (1996), SKS splitting and the seismic anisotropy of the mantle beneath the Hikurangi subduction zone, New Zealand, *Phys. Earth Planet. Int.*, *95*, 227–236.

Gledhill, K., and G. Stuart (1996), Seismic anisotropy in the fore-arc region of the Hikurangi subduction zone, New Zealand, *Phys. Earth Planet. Int.*, *95*, 211–225.

Godfrey, N. J., N. I. Christensen, and D. A. Okaya (2000), Anisotropy of schists: Contribution of crustal anisotropy to active-source seismic experiments and shear wave splitting observations, *J. Geophys. Res.*, *105*, 27,991–28,008, doi:10.1029/2000JB900286.

Godfrey, N. J., F. Davey, T. A. Stern, and D. A. Okaya (2001), Crustal structure and thermal anomalies of the Dunedin Region, South Island, New Zealand, *J. Geophys. Res.*, *106*, 30,835–30,848, doi:10.1029/2000JB000006.

Godfrey, N. J., N. I. Christensen, and D. A. Okaya (2002), The effect of crustal anisotropy on reflector depth and velocity determination from wide-angle seismic data: A synthetic example based on South Island, New Zealand, *Tectonophysics*, *355*, 145–161.

Haines, A. J. (1979), Seismic wave velocities in the uppermost mantle beneath New Zealand, *N. Z. J. Geol. Geophys.*, *22*, 245–257.

International Seismological Centre (2013), On-line bulletin, Internatl. Seis. Cent., Thatcham, U. K. [Available at www.isc.ac.uk.]

Jung, H., and S.-I. Karato (2001), Water-induced fabric transitions in olivine, *Science*, *293*, 1460–1463.

Jung, H., I. Katayama, Z. Jiang, T. Hiraga, and S. Karato (2006), Effects of water and stress on the lattice preferred orientation in olivine, *Tectonophysics*, *421*, 1–22.

Karato, S.-I., H.-Y. Jung, I. Katayama, and P. Skemer (2008), Geodynamic significance of seismic anisotropy of the upper mantle: New insights from laboratory studies, *Annu. Rev. Earth Planet. Sci.*, *36*, 59–95.

Katayama, I., H. Jung, and S.-I. Karato (2004), New type of olivine fabric from deformation experiments at modest water content and low stress, *Geology*, *32*, 1045–1048.

Klosko, E. R., F. T. Wu, H. J. Anderson, D. Eberhart-Phillips, T. V. McEvilly, M. K. Savage, E. Audoine, and K. R. Gledhill (1999), Upper mantle anisotropy in the New Zealand region, *Geophys. Res. Lett.*, *26*, 1497–1500, doi:10.1029/1999GL900273.

Kohler, M. D., and D. Eberhart-Phillips (2003), Intermediate-depth earthquakes in a region of continental convergence: South Island, New Zealand, *Bull. Seismol. Soc. Am.*, *93*, 85–93.

Litchfield, N. J., et al. (2014), A model of active faulting in New Zealand, *N. Z. J. Geol. Geophys.*, *57*(1), 32–56, doi:10.1080/00288306.2013.854256.

Little, T. A., M. K. Savage, and B. Tikoff (2002), Relationship between crustal finite strain and seismic anisotropy in the mantle, Pacific-Australia plate boundary zone, South Island, New Zealand, *Geophys. J. Int.*, *151*, 106–116.

McKenzie, D. (1979), Finite deformation during fluid flow, *Geophys. J. R. Astron. Soc.*, *58*, 689–715.

McKenzie, D., J. Jackson, and K. Priestley (2005), Thermal structure of oceanic and continental lithosphere, *Earth Planet. Sci. Lett.*, *233*, 337–349.

Mei, S., A. M. Suzuki, D. L. Kohlstedt, N. A. Dixon, and W. B. Durham (2010), Experimental constraints on the strength of the lithospheric mantle, *J. Geophys. Res.*, *115*, B08204, doi:10.1029/2009JB006873.

Melhuish, A., W. S. Holbrook, F. Davey, D. A. Okaya, and T. Stern (2005), Crustal and upper mantle seismic structure of the Australian Plate South Island, New Zealand, *Tectonophysics*, *395*, 113–135.

Molnar, P., et al. (1999), Continuous deformation versus faulting through the continental lithosphere of New Zealand, *Science*, *286*, 516–519.

Moore, M., P. England, and B. Parsons (2002), Relation between surface velocity field and shear wave splitting in the South Island of New Zealand, *J. Geophys. Res.*, *107*(B9), 2198, doi:10.1029/2000JB000093.

Morley, A. M., G. W. Stuart, J.-M. Kendall, and M. Reyners (2006), Mantle wedge anisotropy in the Hikurangi subduction zone, central North Island, New Zealand, *Geophys. Res. Lett.*, *33*, L05301, doi:10.1029/2005GL024569.

Nicol, A., C. Mazengarb, F. Chanier, G. Rait, C. Uruski, and L. Wallace (2007), Tectonic evolution of the active Hikurangi subduction margin, New Zealand, since the Oligocene, *Tectonics*, *26*, TC4002, doi:10.1029/2006TC002090.

Nicolas, A., F. Boudier, and A. M. Boullier (1973), Mechanisms of flow in naturally deformed and experimentally deformed peridotites, *Am. J. Sci.*, *273*, 853–876.

Norris, R. J., and A. F. Cooper (2001), Late Quaternary slip rates and slip partitioning on the Alpine fault, New Zealand, *J. Struct. Geol.*, *23*, 507–520.

Pandey, O. P. (1981), Terrestrial heat flow in New Zealand, PhD thesis, p. 194, Victoria Univ. of Wellington, Wellington, New Zealand.

Petersen, T. J., K. Gledhill, M. Chadwick, N. H. Gale, and J. Ristau (2011), The New Zealand National Seismographic Network, *Seismol. Res. Lett.*, *82*, 9–20, doi:10.1785/gssrl.82.1.9.

Raterron, P., Y.-J. Wu, D. J. Weidner, and J.-H. Chen (2004), Low-temperature olivine rheology at high pressure, *Phys. Earth Planet. Inter.*, *145*, 149–159.

Reyners, M. (1987), Subcrustal earthquakes in the central South Island, New Zealand, and the root of the Southern Alps, *Geology*, *15*, 1168–1171.

Reyners, M. (2005), The 1943 Lake Hawea earthquake—A large subcrustal event beneath the Southern Alps of New Zealand, *N. Z. J. Geol. Geophys.*, *48*, 147–152.

Ribe, N. M. (1992), On the relation between seismic anisotropy and finite strain, *J. Geophys. Res.*, *97*, 8737–8747, doi:10.1029/92JB00551.

Ribe, N. M., and Y. Yu (1991), A theory for plastic deformation and textural evolution of olivine polycrystals, *J. Geophys. Res.*, *96*, 8325–8335, doi:10.1029/90JB02721.

Salmon, M., B. L. N. Kennett, T. Stern, and A. R. A. Aitken (2013), The Moho in Australia and New Zealand, *Tectonophysics*, *609*, 283–298, doi:10.1016/j.tecto.2012.07.009.

Savage, M. K., M. Duclos, and K. Marson-Pidgeon (2007a), Seismic anisotropy in South Island, New Zealand, in *A Continental Plate Boundary: Tectonics at South Island, New Zealand*, *Geophys. Monogr.*, vol. 175, edited by D. Okaya, T. Stern, and F. Davey, pp. 95–114, AGU, Washington, D. C.

Savage, M. K., A. Tommasi, S. Ellis, and J. Chery (2007b), Modeling strain and anisotropy along the Alpine Fault, South Island, New Zealand, in *A Continental Plate Boundary: Tectonics at South Island, New Zealand*, *Geophys. Monogr.*, vol. 175, edited by D. Okaya, T. Stern, and F. Davey, pp. 289–305, AGU, Washington, D. C.

Scherwath, M., A. Melhuish, T. Stern, and P. Molnar (2002), *Pn* anisotropy and distributed upper mantle deformation associated with a continental transform fault, *Geophys. Res. Lett.*, *29*(8), 1175, doi:10.1029/2001GL014179.

Scherwath, M., T. Stern, F. Davey, D. Okaya, W. S. Holbrook, R. Davies, and S. Kleffmann (2003), Lithospheric structure across oblique continental collision in New Zealand from wide-angle *P* wave modeling, *J. Geophys. Res.*, *108*(B12), 2566, doi:10.1029/2002JB002286.

Seward, A. M., C. M. Henderson, and E. G. C. Smith (2009), Models of the upper mantle beneath the central North Island, New Zealand, from speeds and anisotropy of subhorizontal *P* waves (*Pn*), *J. Geophys. Res.*, *114*, B01301, doi:10.1029/2008JB005805.

Shi, Y.-L., R. Allis, and F. Davey (1996), Thermal modeling of the Southern Alps, New Zealand, *Pure Appl. Geophys.*, *146*, 469–501.

Shintaku, N., D. W. Forsyth, C. J. Hajewski, and D. S. Weeraratne (2014), *Pn* anisotropy in Mesozoic western Pacific lithosphere, *J. Geophys. Res. Solid Earth*, *119*, 3050–3063, doi:10.1002/2013JB010534.

Smith, G. P., and G. Ekstrom (1999), A global study of *Pn* anisotropy beneath continents, *J. Geophys. Res.*, *104*, 963–980, doi:10.1029/1998JB900021.

Sonder, L. J., and P. England (1986), Vertical averages of rheology of the continental lithosphere: Relation to thin sheet parameters, *Earth Planet. Sci. Lett.*, *77*, 81–90.

Spetzler, J., and R. Snieder (2001), The effect of small-scale heterogeneity on the arrival time of waves, *Geophys. J. Intl*, *145*, 786–796.

Spetzler, J., and R. Snieder (2004), The Fresnel volume and transmitted waves, *Geophysics*, *69*, 653–663.

Sutherland, R. (1995), The Australia-Pacific boundary and Cenozoic plate motions in the SW Pacific: Some constraints from Geosat data, *Tectonics*, *14*, 819–831, doi:10.1029/95TC00930.

Sutherland, R. (1999), Cenozoic bending of New Zealand basement terranes and Alpine Fault displacement: A brief review, *N. Z. J. Geol. Geophys.*, *42*, 295–302.

Sutherland, R., K. Berryman, and R. Norris (2006), Quaternary slip rate and geomorphology of the Alpine fault: Implications for kinematics and seismic hazard in southwest New Zealand, *Geol. Soc. Am. Bull.*, *118*, 464–474.

Townend, J. (1999), Heat flow through the West Coast, South Island, New Zealand, *N. Z. J. Geol. Geophys.*, *42*, 21–31.

Uenzelmann-Neben, G., J. Grobys, K. Gohl, and D. Barker (2009), Neogene sediment structures in Bounty Trough, eastern New Zealand: Influence of magmatic and oceanic current activity, *Geol. Soc. Am. Bull.*, *121*, 134–149, doi:10.1130/B26259.1.

Van Avendonk, H. J. A., W. S. Holbrook, D. Okaya, J. K. Austin, F. Davey, and T. Stern (2004), Continental crust under compression: A seismic refraction study of South Island Geophysical Transect I, South Island, New Zealand, *J. Geophys. Res.*, *109*, B06302, doi:10.1029/2003JB002790.

Vauchez, A., A. Tommasi, and D. Mainprice (2012), Faults (shear zones) in the Earth's mantle, *Tectonophysics*, *558–559*, 1–27.

Walcott, R. I. (1998), Modes of oblique compression: Late Cenozoic tectonics of the South Island of New Zealand, *Rev. Geophys.*, *36*, 1–26, doi:10.1029/97RG03084.

Wallace, L. M., J. Beavan, R. McCaffrey, K. Berryman, and P. Denys (2007), Balancing the plate motion budget in the South Island, New Zealand using GPS, geological and seismological data, *Geophys. J. Int.*, *168*, 332–352.

Warren, J. M., G. Hirth, and P. B. Kelemen (2008), Evolution of olivine lattice preferred orientation during simple shear in the mantle, *Earth Planet. Sci. Lett.*, *272*, 501–512.

Wolfe, C. J., and S. C. Solomon (1998), Shear-wave splitting and implications for mantle flow beneath the MELT region of the East Pacific Rise, *Science*, *280*, 1230–1232.

Zhang, S.-Q., and S.-I. Karato (1995), Lattice preferred orientation of olivine aggregates deformed in simple shear, *Nature*, *375*, 774–777.

Zietlow, D. W., A. F. Sheehan, P. H. Molnar, M. K. Savage, G. Hirth, J. A. Collins, and B. H. Hager (2014), Upper mantle seismic anisotropy at a strike-slip boundary: South Island, New Zealand, *J. Geophys. Res. Solid Earth*, *119*, 1020–1040, doi:10.1002/2013JB010676.